Icarus 390 (2023) 115330

Contents lists available at ScienceDirect

Icarus

journal homepage: www.elsevier.com/locate/icarus

Research Paper

On the co-orbital asteroids in the solar system: medium-term timescale analysis of the quasi-coplanar objects

Sara Di Ruzza [a], Alexandre Pousse [b], Elisa Maria Alessi [b,*]

[a] Università degli Studi di Palermo, Dipartimento di Matematica e Informatica, Via Archirafi 34, 90123, Palermo, Italy
[b] Istituto di Matematica Applicata e Tecnologie Informatiche "E. Magenes", Consiglio Nazionale delle Ricerche (IMATI-CNR), Via Alfonso Corti 12, 20133, Milano, Italy

ARTICLE INFO

Keywords:
Resonances
Orbital
Asteroids
Dynamics
Celestial mechanics
Trojan asteroids

ABSTRACT

The focus of this work is the current distribution of asteroids in co-orbital motion with Venus, Earth and Jupiter, under a quasi-coplanar configuration and for a medium-term timescale of the order of 900 years. A co-orbital trajectory is a heliocentric orbit trapped in a 1:1 mean-motion resonance with a given planet. As such, to model it this work considers the Restricted Three-Body Problem in the planar circular case with the help of averaging techniques. The domain of each co-orbital regime, that is, the quasi-satellite motion, the horseshoe motion and the tadpole motion, can be neatly defined by means of an integrable model and a simple two-dimensional map, that is invariant with respect to the mass parameter of the planet, and turns out to be a remarkable tool to investigate the distribution of the co-orbitals objects of interest. The study is based on the data corresponding to the ephemerides computed by the JPL Horizons system for asteroids with a sufficient low orbital inclination with respect to the Sun–planet orbital plane. These objects are cataloged according to their current dynamics, together with the transitions that occur in the given time frame from a given type of co-orbital motion to another. The results provide a general catalog of co-orbital asteroids in the solar system, the first one to our knowledge, and an efficient mean to study transitions.

1. Introduction

The co-orbital motion is a particular type of dynamics according to which two bodies (e.g., an asteroid and a planet) orbit the same central body (e.g., Sun) in the same period. Many objects susceptible to be at least temporary co-orbitals have been observed in the solar system. Earth, Venus, Mars and Jupiter are the planets with the largest number of documented co-orbital objects, while Saturn, Neptune and Uranus possess at least one object of this type (see, e.g., Gallardo, 2006). A major example is given by the Trojans of Jupiter. These asteroids are observed since the 1900s on tadpole-shaped (TP) trajectories (Wolf, 1906) in the neighborhood of the two Lagrange equilateral equilibrium points L_4 and L_5 in the synodic reference system. Another illustrative case is given by the moons Janus and Epimetheus that orbit Saturn on quasi-coplanar and quasi-circular trajectories. As their orbital periods are slightly different, the inner moon catches up with the outer one, and their mutual gravitational influence leads to a swapping of the orbits every 4 years (the satellite on the outer path moves to the inner one and vice versa, see Murray and Dermott, 2000), as confirmed by Voyager 1 (Aksnes, 1985). In the synodic reference system, they follow horseshoe-shaped (HS) trajectories. Several near-Earth asteroids have been observed with a similar behavior. For instance, 2013 BS45 orbits the Sun in about one year on a low eccentric quasi-planar trajectory and experiences regular close encounters with the Earth every 80 years (de la Fuente Marcos and de la Fuente Marcos, 2013). If, instead, the asteroid orbits around the Sun in such a way that the Sun's and the planet's gravitational accelerations act to create an asteroid retrograde motion with respect to the planet in the rotating frame, we speak of quasi-satellite (QS) orbit. The first confirmed body in QS motion was 2002 VE68 harbored by Venus (Mikkola et al., 2004). QS, HS and TP motions are not necessarily stable over long times, and, in particular, transitions from one dynamic to another can occur. An important example in recent years is given by the near-Earth asteroid 2016 HO3, also called Kamo'oalewa, a co-orbital of the Earth which is currently in QS motion, but that was in HS state in the past and will become so again in several centuries (de la Fuente Marcos and de la Fuente Marcos, 2016). Finally, in the case of inclined orbits with respect to the planet orbital plane, Namouni (1999) and Namouni et al. (1999) described compound trajectories denoted HS-QS, TP-QS or TP-QS-TP, that correspond to a stable coexistence of, at least, two co-orbital behaviors. According to the authors, the compound regime is

* Corresponding author.
E-mail addresses: sara.diruzza@unipa.it (S. Di Ruzza), poussealexandre@gmail.com (A. Pousse), elisamaria.alessi@cnr.it (E.M. Alessi).

https://doi.org/10.1016/j.icarus.2022.115330
Received 9 August 2022; Received in revised form 18 October 2022; Accepted 21 October 2022
Available online 26 October 2022

a new type of co-orbital motion, and thus dynamically different to the one-time transitions described for 2016 HO3. The same authors also mentioned the passing orbits, that are inclined and non-resonant orbits located in the neighborhood of the region of co-orbital motion in the phase space. This type of dynamics is not considered in this paper.

On the other hand, co-orbital trajectories, the possible transitions between them, together with escaping/trapping mechanisms, are considered as novel solutions for space retrieval and exploration missions. For instance, the JAXA-CNES MMX mission, aimed at the exploration of the Martian moons, plans to place a probe on a QS orbit at Phobos (Nakamura et al., 2021). Moreover, ESA is planning to exploit the neighborhood of L_5 of the Sun–Earth system to monitor the solar activity and the related space weather issues (ESA, 2022). As an additional example, the Chinese space agency is intended to visit the asteroid Kamo'oalewa, which is exceptional due to its long-term QS state (Gibney, 2019; Jin et al., 2020).

As it was implicitly assumed in the description above, since the masses of the considered objects (e.g., asteroids or spacecraft) are significantly smaller than the mass of the two other bodies involved in the problem (i.e., Sun and planet), the Restricted Three-Body Problem (RTBP) is the classical model for describing the co-orbital motion. In particular, the corresponding area of the phase space can be tackled through the perturbation theory, with the help of averaging techniques. The averaged problem of the 1:1 mean-motion resonance has the advantage to be integrable in the planar circular case, thus providing a complete understanding of the co-orbital resonance. In this context, the domain of each dynamical regime in the phase space can be neatly defined (Nesvorný et al., 2002; Pousse and Alessi, 2022).

The objective of this work is to show how the integrable approximation obtained with the help of the classical tools of dynamical systems theory and perturbation techniques can be applied to describe the dynamics of real natural objects in the solar system, and to see what we can learn from their behavior to improve the analytical description.

To the best of our knowledge, there exist only official catalogs of Trojan asteroids of Earth, Mars, Jupiter, Uranus and Neptune (Minor Planet Center, 2022), while for other co-orbital motions there exist only works that focus specifically on given objects (see, e.g., Mikkola et al., 2004; Brasser et al., 2004; Kinoshita and Nakai, 2007; Wajer, 2010; Wajer and Kròlikowska, 2012; de la Fuente Marcos and de la Fuente Marcos, 2012, 2016). Contrary to the classical studies that investigate the stability on secular timescales, from several millennia to million years (see, e.g., Ćuk et al., 2012; Robutel and Gabern, 2006, for studies on HS and TP, respectively) the co-orbital motion is investigated here in a medium timescale, of the order of several centuries. More precisely, the analysis is based on the ephemerides computed by the JPL Horizons system (NASA, 2022), covering a time span of the order of 900 years. This constraint in time together with the features of the co-orbital motion leads us to restrict the study to the co-orbitals of Venus, Earth and Jupiter.

In addition, in order to remain close to the domain of validity of the integrable approximation, only the asteroids whose orbit can be considered, within a certain threshold, on the orbital plane of the given planet will be analyzed. They will be referred as asteroids in "quasi-planar" co-orbital motion with the given planet.

By using the data obtained on the basis of real observations, the theory will be linked to the experimental data, showing whether the integrable approximation is a relevant model in order to describe the co-orbital asteroids in the considered time frame. Moreover, some conclusions on the future directions to be taken to improve the averaged model, especially in the three-dimensional case, will be drawn. In particular, one of the goals is to highlight the transitions from a given type of dynamics to another, showing the ones that can be ascribable to the integrable approximation within its limit of validity, and those that are not.

It is worth mentioning a recent paper by Qi and Qiao (2022), where an analysis of Earth co-orbital asteroids is performed. The authors consider the spatial case and they aim to study the dynamical stability of the objects on a long timescale. They use a two-dimensional map, by considering the inclination and the value of the energy (given by the averaged Hamiltonian), and they divide the phase space in several regions identifying the co-orbital dynamics. Then, they perform an analysis of the stability of such regions. On the medium timescale, our results are in agreement with their work.

This work is organized as follows. Without too much detail, the perturbation scheme that leads to the averaged problem is explained in Section 2, together with the tool developed in the planar circular case. In Section 3, the data considered are described. In Section 4, the results obtained for each Sun–planet system taken into account are given. In Section 5, conclusions and future directions are highlighted.

2. The averaged problem in the planar circular case

For the sake of clarity, we summarize here the reasoning that leads to the integrable approximation of the co-orbital resonance and refer the reader to Pousse and Alessi (2022) for the full derivation and analysis.

The model is based on the RTBP, that is, the study of the motion of a massless body (a particle, an asteroid or a spacecraft), affected by the gravitational attraction of the Sun and a planet. In that framework, the motion of the two massive bodies follows a solution of the two-body problem, and, in the circular case, the planet and the Sun move on a circular orbit around their barycenter. The following Hamiltonian function provides the dynamics of the problem in the heliocentric reference frame:

$$\mathcal{H}\left(\mathbf{r},\dot{\mathbf{r}},\lambda_p\right)=\frac{\|\dot{\mathbf{r}}\|^2}{2}-\frac{\mu}{\|\mathbf{r}\|}-\frac{(\mu+\mu_p)\varepsilon}{\left\|\mathbf{r}-\mathbf{r}_p\left(\lambda_p\right)\right\|}+(\mu+\mu_p)\varepsilon\mathbf{r}\cdot\mathbf{r}_p\left(\lambda_p\right) \tag{1}$$

where μ and μ_p are the respective mass parameter of the Sun and the planet,

$$\varepsilon:=\frac{\mu_p}{\mu+\mu_p},$$

is a dimensionless parameter characterizing the mass ratio of the Sun–planet system, the vectors $\mathbf{r},\dot{\mathbf{r}}\in\mathbb{R}^2$ are canonical variables corresponding to the position and the velocity of the particle and $\|\cdot\|$ is the Euclidean norm associated with the scalar product denoted $\cdot$. In the planar case, the motion of the particle takes place on the orbital plane of the planet. The heliocentric vector $\mathbf{r}_p(\lambda_p)$ denotes the position of the planet for a given value of the mean longitude $\lambda_p=M_p+\varpi_p$, whose evolution is proportional to time with an angular velocity – generally known as mean-motion – that reads

$$n_p:=\sqrt{\frac{\mu+\mu_p}{a_p^3}}$$

being a_p, M_p and ϖ_p its semi-major axis, its mean anomaly and its longitude of the periastron, respectively.

The problem is usually analyzed in the synodic reference system, that rotates together with the planet. In this system, the planet is located at $a_p(1-\varepsilon,0)$, while the Sun at $a_p(-\varepsilon,0)$. In the synodic reference system, it is well known that there exist 5 equilibrium points, called the *Lagrangian points*, denoted as L_j, $(j=1,\dots 5)$ and that a first integral of the problem can be defined, the so-called *Jacobi constant*. The dynamics of interest for this work are connected to some relevant families of periodic orbits that exist in the synodic reference frame (Szebehely, 1967). For instance, the HS motion is associated with the hyperbolic invariant manifolds of the Lyapunov family $\mathscr{L}_3$ that stems from L_3 (Barrabés and Ollé, 2006), while the TP motion arises from the neighborhood of $\mathscr{L}_j^s$ and $\mathscr{L}_j^l$, that are the two Lyapunov families of L_j for $j=4,5$, generally known as the short and long periodic families, due to their associated timescale in the neighborhood of the equilibrium point. The QS regime is remarkable for the fact that it is not

connected to the Lagrange points, but stems from a family of simple-periodic symmetrical retrograde satellite orbits generally known as the family f (see, e.g., Pousse et al., 2017, for more details). According to the Poincaré classification these families of periodic orbits are the continuation, from the limit case $\varepsilon = 0$, of heliocentric Kepler orbits in 1:1 mean-motion resonance with the planet. Consequently, a natural choice of perturbative treatment in order to recover these structures is to consider ε as a small parameter.

For ε small enough, the Hamiltonian in Eq. (1) can be split as

$$\mathcal{H}\left(\mathbf{r}, \dot{\mathbf{r}}, \lambda_p\right) = \mathcal{H}_{\mathrm{K}}\left(\mathbf{r}, \dot{\mathbf{r}}\right) + (\mu + \mu_p)\varepsilon \mathcal{H}_{\mathrm{P}}\left(\mathbf{r}, \lambda_p\right),$$

where $\mathcal{H}_{\mathrm{K}}$ corresponds to the Kepler motion around the Sun, while $\mathcal{H}_{\mathrm{P}}$ models the perturbations which derive from the gravitational effect of the planet. In the unperturbed problem, that is for $\varepsilon = 0$, the particle lies on an ellipse that can be defined by the orbital elements (a, e, ϖ) (semi-major axis, eccentricity, longitude of the periastron, respectively). The position on its ellipse can be obtained through several angles: the true anomaly v, the mean anomaly M or the mean longitude $\lambda = M + \varpi$, a fictitious angle proportional to time such that

$$\dot{\lambda} = \sqrt{\frac{\mu + \mu_p}{a^3}}.$$

Therefore, the commensurability associated with the 1:1 mean-motion resonance occurs for a semi-major axis equals to a_p.

In order to focus on the co-orbital resonance, one can define the resonant angle

$$\theta := \lambda - \lambda_p,$$

as well as its conjugated dimensionless action

$$u := \sqrt{\frac{a}{a_p}} - 1,$$

whose modulus measures the distance to the commensurability, such that $\dot{\theta}$ is equal to zero at the resonance in the unperturbed problem, that is, for $u = 0$. Hence, studying the co-orbital resonance in that perturbative frame consists in understanding how the perturbation $\mathcal{H}_{\mathrm{P}}$ transforms the unperturbed phase space in the neighborhood of $u = 0$. All the variables (θ, u, e, ϖ) might vary and this makes the motion difficult to understand; nevertheless, for ε and $|u|$ small enough, the angular variables θ and ϖ evolve at different rates with respect to the "fast" angle λ_p. More precisely, θ undergoes "semi-fast" variations corresponding to the resonant dynamics while ϖ experiences a "secular" drift. A classical way to exploit this feature is to replace the original Hamiltonian by one in which the fast oscillations are removed. This process defines the averaged problem in the co-orbital resonance. In a more practical way, the averaged Hamiltonian is obtained by replacing the mean longitude λ by $\theta + \lambda_p$, and implementing an averaging with respect to the fast angle λ_p. For further details the reader is referred to the work of Nesvorný et al. (2002), that develops a semi-analytical method in order to compute the averaged Hamiltonian as well as its derived equations of motion, and thus provides an integrator for co-orbital trajectories.

Finally, an important feature occurs in the planar circular case: the invariance of $\mathcal{H}$ under the group of rotations SO(2) in the plane implies that the averaged Hamiltonian does not depend on ϖ while the quantity

$$\Gamma := \sqrt{a}(1 - \sqrt{1 - e^2})$$

is a first integral. Hence for various values of Γ, seen as a parameter, the averaged Hamiltonian $\overline{H}^{\Gamma}(\theta, u)$ is integrable and allows to understand the global dynamics of the 1:1 mean-motion resonance through a simple description of phase portraits in the resonant variables (θ, u).

2.1. Phase portraits description and (θ, e)-map of the co-orbital resonance

For a given $0 \leq \Gamma < \sqrt{a_p}$, the averaged Hamiltonian is integrable with one degree of freedom and a phase portrait can be computed. The co-orbital trajectories are solutions located in the neighborhood of $u = 0$ and such that θ oscillates around a given value. Only three types of co-orbital dynamics exist in the planar circular case: the quasi-satellite regime where θ librates around zero for $\Gamma > 0$, the tadpole motion of L_j with $j = 4, 5$ where θ experiences a periodic oscillation around a given $\theta_j(\Gamma)$ satisfying $23.9° < (-1)^j \theta_j(\Gamma) < 180°$, and the horseshoe trajectories where θ oscillates around 180° with a large amplitude that decreases as long as Γ increases.

For instance, Fig. 1 displays a phase portrait in the case of the Sun–Earth system with $\Gamma = \sqrt{a_p}(1 - \sqrt{1 - e^2})$ and $e = 0.15$. The phase portrait has four equilibrium points represented on the figure by crosses. The elliptic equilibrium points located in the neighborhood of $(\theta, u) = ((-1)^j 60°, 0)$ for $j = 4, 5$ stand for periodic orbits of $\mathscr{L}_4^s$ and $\mathscr{L}_5^s$, while the elliptic equilibrium point located close to the origin is associated with a periodic orbit of the family f. Therefore, the trajectories that librate around them, are respectively, the TP of L_4, the TP of L_5, and the QS. The hyperbolic equilibrium point located at $\theta = 180°$ and $u \simeq 0$ corresponds to a periodic orbit that belongs to $\mathscr{L}_3$. A separatrix, represented by the red dashed curve, emerges from it and approximates the corresponding stable and unstable invariant manifolds. Besides, the separatrix bounds the two TP regions, giving rise to the HS trajectories that encompass it. Finally, the two black dashed lines embody the collision with the Earth where the averaged Hamiltonian is not defined, and delimit the domains of QS and HS motion.

In the case of quasi-circular orbits, that is for $\Gamma = 0$, the resonant angle θ coincides with the angular separation between the particle and the planet, denoted ϕ, while the heliocentric norm, denoted R, is equal to $a = a_p(1 + u)^2$. Hence, in the synodic reference frame for which the Sun is at the origin and the planet is located in $(a_p, 0)$, the motion of the particle is equivalent to the following trajectory:

$$(X(t), Y(t)) = a_p(1 + u(t))^2(\cos\theta(t), \sin\theta(t)). \tag{2}$$

For $\Gamma > 0$, Eq. (2) does not provide the motion of the particle in the synodic reference frame, but the dynamics of its guiding center, a concept that is used in literature to describe the resonant behavior of a co-orbital trajectory (see, e.g., Namouni, 1999; Murray and Dermott, 2000).

In order to model the trajectory in the synodic reference frame, it is necessary to take into account the degree of freedom (e, ϖ). Due to the conservation of Γ, $e(t)$ undergoes semi-fast oscillations around a value $e_0 = \sqrt{1 - (1 - \Gamma)^2}$ which corresponds to the eccentricity for $u = 0$, while $\varpi(t)$ experiences a secular drift combined with the oscillations generated by the resonant behavior. Besides, the transformation from the orbital elements to the synodic reference frame introduces a fast oscillation generated by the angle $\lambda_p(t)$.

Hence, in first approximation, the motion of the particle can be written as follows:

$$(X(t), (Y(t))) = R(t)(\cos\phi(t), \sin\phi(t))$$

with

$$R(t) = a_p(1 - e_0 \cos M(t)), \quad \phi(t) = \theta(t) + e_0 F(M(t))$$

where $M(t) = M(0) + (n_p - g)t$ is the mean anomaly of the particle, g is the frequency of the secular drift in ϖ, and F is a 2π-periodic function derived from the difference between the true anomaly v and M.

As a consequence, a periodic solution $(\theta(t), u(t))$ of a given phase portrait provides a quasi-periodic trajectory in the synodic reference frame that results from the combination of a fast oscillation of frequency $n_p - g$, whose amplitude is related to the eccentricity, and a slower oscillation generated by the resonant behavior embodied by the guiding center.

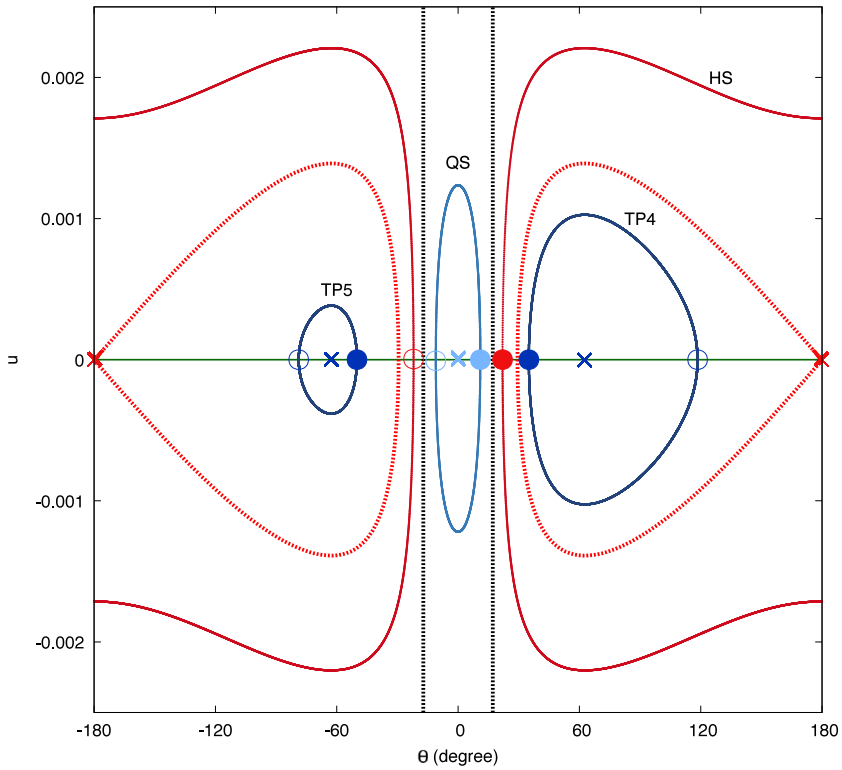

Fig. 1. Phase portrait of the averaged Hamiltonian for a Sun–Earth system and $\Gamma = \sqrt{a_p}(1-\sqrt{1-e^2})$ with $e = 0.15$. The black dashed lines represent the collision with the planet. The blue, sky blue and red trajectories are level curves associated with TP orbits of L_4 and L_5, QS and HS motion, respectively. The blue and sky blue crosses are elliptic equilibrium points. More precisely, they correspond, respectively, to periodic orbits of the family $\mathscr{L}_j^s$ for $j = 4, 5$ and f. The red crosses are a hyperbolic equilibrium point associated with a periodic orbit of $\mathscr{L}_3$ and from which emerges a separatrix (the red dashed curve) that bounds the two domains of TP motion and the one of the HS motion. The green line corresponds to the section $u = 0$. Each periodic solution of the phase portrait crosses the section $u = 0$ in two points, represented by colored disks and circles on the phase portrait. (For interpretation of the references to color in this figure legend, the reader is referred to the web version of this article.)

For instance, Fig. 2b–d display, respectively, the TP, HS and QS orbits of Fig. 1 (gray dots) as well as the evolution of their guiding center (colored curves). Finally, as depicted in Fig. 2a, for an equilibrium point of Fig. 1, the corresponding trajectory in the synodic reference frame (colored curves) is the one of a periodic orbit while its guiding center is a fixed point (colored crosses).

The topology of the phase portraits evolves by increasing Γ. Inside the collision curve, the size of the QS domain increases until it dominates the phase portrait for high values of Γ. Outside the collision curve, the two elliptic equilibrium points get closer to the hyperbolic fixed point, therefore the TP domains shrink and vanish when the three merge. More generally, for all $0 \leq \Gamma < \sqrt{a_p}$, each domain of dynamics extends quasi-symmetrically with respect to the axis $u = 0$ and is neatly defined by the collision curve or the separatrix. Therefore, their crossings with the section $u = 0$, that is $a = a_p$, provides a compact way to understand the global evolution of the different domains of dynamics by varying Γ, or equivalently, by varying the eccentricity of the orbit.

Fig. 3 displays the (θ, e)-map of the co-orbital resonance in the case of a Sun–Earth system. The black and red thick curves $|\theta| = \Theta_{col}(e)$ and $|\theta| = \Theta_{sep}(e)$, depict, respectively, the crossings of the collision curve and of the separatrix with the section $u = 0$, for all $0 \leq e < 1$. Note that $\Theta_{col}(e)$ can be approximated by $2e$ up to high values of eccentricities while, according to the classical result (Garfinkel, 1977), $\Theta_{sep}(0) \simeq 23.9°$. In this framework, each type of dynamics belong to one of the following domains:

$$\begin{aligned} \mathcal{D}_{QS} &= \{|\theta| < \Theta_{col}(e)\}, \\ \mathcal{D}_{HS} &= \{\Theta_{col}(e) < |\theta| < \Theta_{sep}(e)\}, \\ \mathcal{D}_{TP_j} &= \{\Theta_{sep}(e) < (-1)^j \theta < 180°\}. \end{aligned} \tag{3}$$

Hence, for a given eccentricity e when the particle is at the resonance, a periodic solution $(\theta(t), u(t))$ intersects the section in exactly two values of θ, that belong to one of the three domains of Eq. (3), on both sides of a curve that represents a family of equilibrium points, that is, $\mathscr{L}_4^s$ or $\mathscr{L}_5^s$ for the TP, f for the QS and $\mathscr{L}_3$ for the HS. These two crossings $(\theta_j, e)_{j=1,2}$ are identified by colored disks and circles on Fig. 1, and Fig. 3, as well as on Fig. 2b–d.

As a consequence, the averaged problem in the planar circular case, through the (θ, e)-map, provides a simple method to identify the type of motion of co-orbital trajectories. Besides the tool given by the (θ, e)-map of Fig. 3 does not apply only to the Sun–Earth system, as it is invariant with respect to ε. This remarkable feature derives to the fact that the following rescaling $\sqrt{\varepsilon}^{-1}\overline{H}^{\Gamma}(\theta, \sqrt{\varepsilon}u)$ makes the averaged Hamiltonian independent of ε. Hence, as long as ε can be considered as a small parameter, that is the case for all the Sun–planet systems of the solar system, the (θ, e)-map of Fig. 3 is reliable to identify the type of dynamics of the co-orbital motion.

2.2. On the validity limit of the model

The averaged problem in planar circular case has some limits of validity which might constrain its application to real objects in the solar system. The first one derives from the perturbative treatment. Indeed, according to the perturbation theory, the averaging process coincides with the existence of a symplectic transformation which maps the original Hamiltonian to the averaged Hamiltonian plus a remainder that is supposed to be small and thus dropped in the averaged problem. As long as the planet and the particle are getting closer, the remainder can increase and can no longer be considered negligible with respect to the averaged perturbation in $\overline{H}^{\Gamma}$. Through a rigorous treatment, Pousse and Alessi (2022) proved that the model and the (θ, e)-map are reliable as long as the considered trajectories lay outside the Hill's sphere of the planet. More precisely, the dropped remainder generates a perturbation

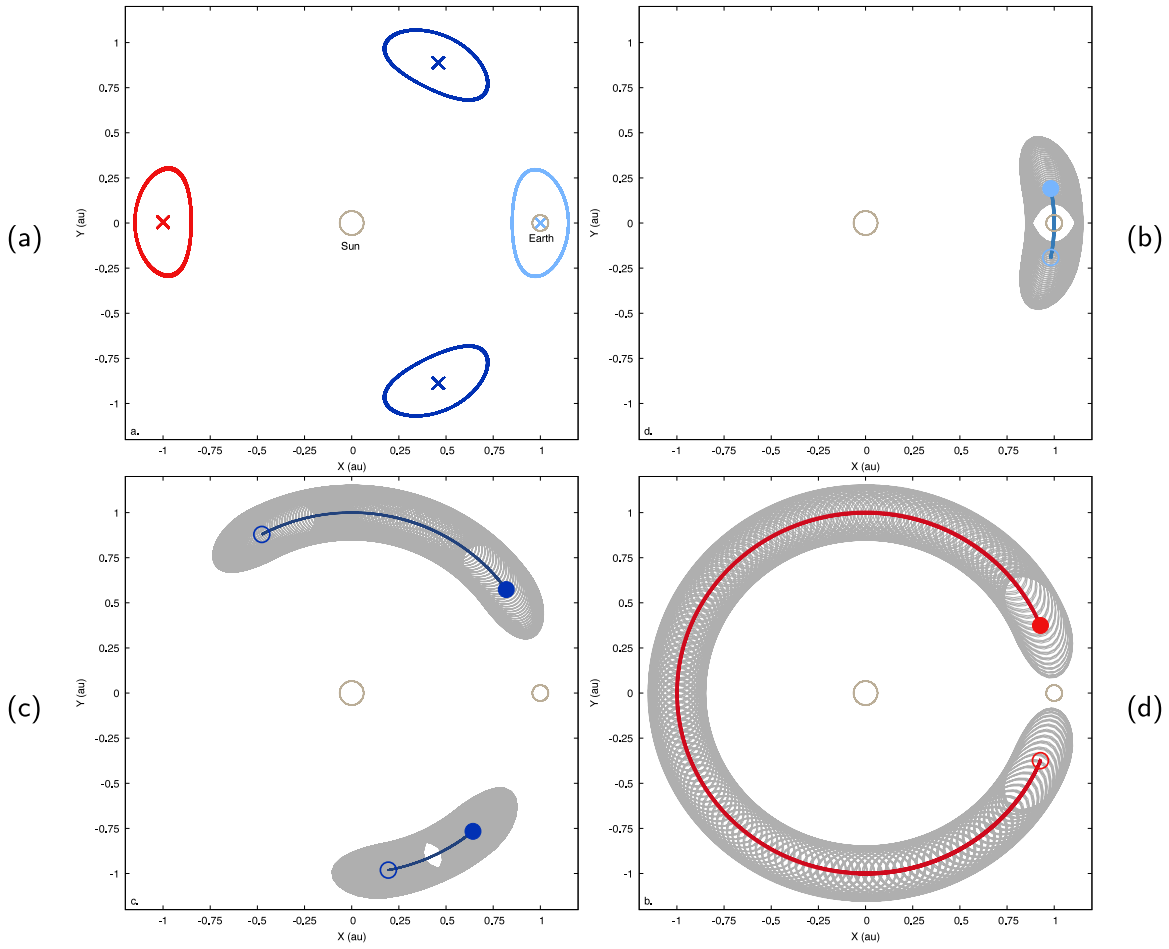

Fig. 2. Trajectories in the synodic reference frame propagated with the integrator of the averaged problem, for 500 years. The Sun is at the origin and the Earth is located at $(1, 0)$. Panel (a): Periodic orbits and respective guiding center (red, blue, sky blue crosses) associated with the four equilibrium points of the phase portrait of Fig. 1. Panels (b) (c) and (d): trajectories (gray dots) corresponding respectively to the QS, TP and HS orbits of Fig. 1. The thick colored curves embody the evolution of their respective guiding center while the colored disks and circles represent the crossings with the section $u = 0$. (For interpretation of the references to color in this figure legend, the reader is referred to the web version of this article.)

whose size increases as the distance to the planet decreases, tending to the Hill's radius, which may destabilize the quasi-periodic character of the co-orbital trajectories described in the averaged problem. In the framework of the (θ, u)-map, it is expected that the crossings of a co-orbital trajectory slowly drift such that transitions from a given domain to another are possible, especially for crossings located close to the collision curve or in the neighborhood of the separatrices. Nevertheless, since these instabilities occur in the framework of the RTBP in circular-case, they conserve the Jacobi constant.

Another limit of validity of the model is given by the RTBP in planar circular case itself. Real objects are not co-planar with the planet, therefore it is necessary to define an arbitrary threshold in order to distinguish the quasi-coplanar trajectories. According to Namouni (1999), Nesvorný et al. (2002), the effect of the inclination may generate transitions, escapes and also new types of co-orbital dynamics, as for instance the compound orbits mentioned in the Introduction (see also Section 4.1 for a discussion on this dynamics).

Finally, other effects may have a role on the dynamics of real objects, such as the eccentricity of the planet, possible close encounters with other massive objects or non-gravitational forces as the solar radiation pressure. In these situations, the Jacobi constant is no longer conserved. For possible close encounters with other planets, an indication can be obtained by assuming that all the planets of the solar system move in the same plane on circular orbits and estimating the eccentricities corresponding to the crossing of the orbit of the inner planets (at perihelion), and of the outer planets (at aphelion), with respect to the considered Sun–planet system. In principle, an asteroid that crosses the orbit of another planet will do it twice per orbital period and the corresponding gravitational effect cannot be neglected over long timescales.

Table 1
For each Sun–planet system, ϵ is the mass parameter, T_{rev} is the period of revolution of the planet, T_{lib} is the period of libration of θ in the neighborhood of L_4 or L_5, and N_{lib} the number of librations possibly performed in 900 years. All the periods are reported in years. The physical values are taken from NASA JPL Solar System Dynamics (2022a).

Planet	ϵ	T_{rev}	T_{lib}	N_{lib}
Mercury	$1.66012055 \times 10^{-7}$	0.24	227.51	3.95
Venus	$2.44783229 \times 10^{-6}$	0.61	151.34	5.95
Earth	$3.00348059 \times 10^{-6}$	1.00	222.09	4.05
Mars	$3.22715504 \times 10^{-7}$	1.88	1274.36	0.71
Jupiter	$9.53881152 \times 10^{-4}$	11.87	147.88	6.09
Saturn	$2.85803962 \times 10^{-4}$	29.47	671.02	1.34
Uranus	$4.36605898 \times 10^{-5}$	84.05	4896.06	0.18
Neptune	$5.15111841 \times 10^{-5}$	164.89	8842.75	0.10

3. JPL horizons medium-term ephemerides

The test bench for the integrable model presented above is given by the ephemerides of asteroids computed by the JPL Horizons system (NASA, 2022).

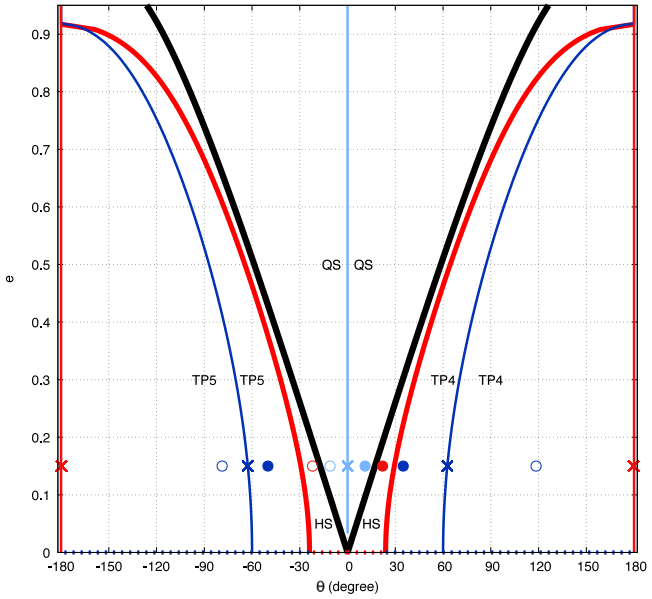

Fig. 3. The (θ, e)-map of the co-orbital motion defined by the section $u = 0$. The black and red thick curves stand, respectively, for the singularity of collision and the crossing of the separatrices that originate from L_3 (thick red curve). They divide the map in three regions. The QS and TP domains are centered, respectively, on the family f (sky blue curve) and the short periodic families $\mathscr{L}_j^s$ (blue curves). The HS region is split in two parts, between the separatrix and the curve associated with the collision. The crosses, colored disks and circles denote the crossings of the solutions $(\theta(t), u(t))$ plotted in the phase portrait of Fig. 1. (For interpretation of the references to color in this figure legend, the reader is referred to the web version of this article.)

Table 2
Range of semi-major axis (in au) for the possible asteroids to be analyzed. The orbit parameters are taken from NASA JPL SSD (2022b).

Planet	a_p	$[a_{\min}, a_{\max}]$
Venus	0.72332102	$a_p \pm 2.7\%$
Earth	1.00000018	$a_p \pm 2.9\%$
Jupiter	5.20248019	$a_p \pm 19.7\%$

The analysis starts from the choice of the Sun–planet systems that can be addressed and of the small bodies that may follow a quasi-coplanar co-orbital motion in such systems. The asteroids are first filtered according to their semi-major axis and inclination, to fulfill the condition of being in 1:1 mean-motion resonance with the given planet, and to orbit on a quasi-coplanar configuration with respect to the Sun–planet reference plane.

3.1. On the selection of the sun–planet systems and the asteroids

The maximum time span covered by the ephemerides computed by the JPL Horizons system for small bodies is 900 years, from 1599-12-10 23:59 to 2500-12-31 23:58 (NASA JPL SSD, 2022c). According to that, it is necessary to estimate for each planet if the characteristic period associated with the resonant behavior can be revealed in this time span. The period of libration of θ in the neighborhood of L_4 or L_5, that is (Garfinkel, 1977)

$$T_{lib} = \frac{2\pi}{n_p}\sqrt{\frac{27}{4}\varepsilon}^{-1}\,(1+\mathcal{O}(\varepsilon)),$$

is introduced as a period of reference to this end. Only the planets such that an asteroid can perform at least two librations in 900 years are considered.

In Table 1, the number of years corresponding to one libration is reported for each Sun–planet system as well as the number of librations in the considered time frame. From the data shown, the Sun–planet systems that fulfill the given criterion are the ones associated with Mercury, Venus, Earth and Jupiter. However, since the orbit of Mercury is significantly eccentric ($e_p \simeq 0.2$), the case of the Sun–Mercury system has been removed from the study.

Regarding the choice of the asteroids to be considered, it is necessary to define an admissible range of semi-major axis located in the neighborhood of the resonance, that is $a = a_p$. To this end, we use the thresholds given by the separatrices that stem from L_1 and L_2 in the averaged problem for quasi-circular orbits (i.e., $\Gamma = 0$) and bound the co-orbital region (see Pousse and Alessi, 2022). Following the same reasoning as in Robutel and Pousse (2013), it can be shown that the co-orbital motion is located in the following subset of the phase space in terms of resonant action:

$$|u| < \varepsilon^{1/3}.$$

For the planets considered in this study, it corresponds to the range of semi-major axis $[a_{\min}, a_{\max}]$ shown in Table 2.

Finally, the condition of co-planarity required by the model is considered as fulfilled for all the asteroids that orbit the Sun with an inclination with respect to the ecliptic plane, denoted I^{ecl}, that satisfies

$$I^{ecl} - I_p^{ecl} < 10°,$$

where I_p^{ecl} denotes the inclination of the planet to the ecliptic. From a geometric point of view, the two inclinations do not subtract, unless Ω^{ecl} and Ω_p^{ecl}, respectively the longitude of the node of the asteroid and of the planet with respect to the ecliptic reference system, coincide. The above assumption is a technical choice, in order to simplify the filtering. Notice that only asteroids with a prograde motion are studied.

We point out that the inclination threshold is set arbitrarily as a preliminary criterion to define quasi-coplanarity and to test the usefulness of the planar circular model in investigating the distribution of co-orbital objects in the solar system. The definition of quasi-coplanarity will be refined in a future work. In particular, we expect a criterion that depends on the mass ratio of the considered Sun–planet system.

3.2. Methodology

The asteroids whose motion is analyzed are taken from the website of the NASA JPL SSD Small-Body Database (2022), as the ones satisfying the conditions defined above at the date of 2021-03-21 00.00.00 (JD 2459294.50). Then, through the API service of the JPL Horizons system, the heliocentric osculating Cartesian coordinates are computed in the IAU76/J2000 ecliptic reference system for each of such asteroids and for the nominal planet for the maximum timescale available that depends on the planet and the specific object.

In order to apply the model and take advantage of the (θ, e)-map, the orbital elements must be defined with respect to the planet orbital plane rather that the ecliptic. Thus, a set of three orthogonal rotations are applied to the position and velocity vectors of the object to change its coordinates from the ecliptic to the orbital reference frame of the planet.

Let X^{ecl} and X be the three-dimensional state vector of the asteroid in the ecliptic and in the orbital reference frame of the planet, respectively. Then, the following coordinate change is applied:

$$X = \mathcal{R}_z(-\omega_p^{ecl})\mathcal{R}_x(-I_p^{ecl})\mathcal{R}_z(-\Omega_p^{ecl})X^{ecl}$$

where ω_p^{ecl}, is the argument of periastron of the planet, while the matrix $\mathcal{R}_k(\alpha)$ is the orthogonal rotation about the k-axis of an angle α.

Finally, from X, the orbital elements of the asteroid and of the planet are computed in the new reference system (Bate et al., 1971). Notice that in this way, osculating orbital elements are computed in the osculating orbital plane of the planet.

Once computed the orbital elements in the suitable reference system, then the algorithm looks for the possible intersections of the variable $u = \sqrt{a/a_p} - 1$ with zero. If this condition – assumed to be the *co-orbital condition* – occurs, then also the corresponding (θ, e) are

computed and stored. Concerning θ, it is computed as the difference between the two osculating longitudes in the orbital plane of the planet as

$$\theta = (M + \varpi) - (M_p + \varpi_p)$$

with the longitude of the periastron $\varpi = \Omega + \omega$ where ω and Ω denotes respectively the argument of periastron and the longitude of the node in the orbital plane of the planet.

4. Analysis

This section describes the co-orbital objects found for each planet, showing common features both in case their number is small, as for the case of Venus, and in case their number is very high, as for Jupiter.

Fig. 4a–c displays the (θ, e)-maps for the three planets, respectively, Venus, Earth and Jupiter. The points in magenta represent the distribution of co-orbital asteroids in the (θ, e)-map at the current date, while the two horizontal lines stand for the eccentricities of an object in co-orbital motion with the considered planet P when it crosses the orbit of an inner and an outer planet (respectively in green and purple) with respect to P.

Let us start with the analysis of Venus (Fig. 4a). The horizontal lines in purple and green, corresponding to the eccentricity values of $e = 0.38$ and $e = 0.37$, are associated with the crossing with the Earth's and Mercury's orbit, respectively. Most of the objects found are along or above these lines with a significant eccentricity. This peculiar distribution opens the question on whether it can be an observational bias due to the greater ease of detecting such objects, while asteroids in co-orbital motion with Venus orbiting within the Earth's orbit are always close to the Sun and always have a small elongation, so it is difficult to detect them from Earth through optical instruments (we refer to Sheppard et al. (2022) for recent results of a survey of asteroids interior to Earth and Venus). A different explanation can be a dynamical mechanism generated by Venus together with Earth or Mercury.

Fig. 4b shows the objects in co-orbital motion with the Earth. The green and purple horizontal lines in $e = 0.28$ and $e = 0.52$ correspond to the possible crossings with the orbit of Venus and Mars, respectively. Most of the detected asteroids are close to the lines corresponding to the singularities generated by the collision with the Earth in the integrable model, that is, the line that separates the domain of the QS motion from the HS one. Moreover, most of the co-orbital objects has eccentricities lower than the ones of the crossing with Venus and Mars. For the same reason as for the co-orbital objects of Venus, such distribution may be due to the ease of detecting asteroids that experience relatively close encounters with the Earth, which is the case for QS with low eccentricities and HS trajectories. In Fig. 5, we show the evolution of Earth's co-orbitals, that is, all the domains concerned by the asteroids analyzed. The specific distribution close to the singularity curves seem to confirm the observational bias, but also an unstable character of the Earth's co-orbitals can be considered to explain the figure. At the moment, however, the time span investigated cannot allow to say this with certainty, nor we have a rigorous dynamical argument in favor of the latter thesis.

Fig. 4c displays the (θ, e)-map of the asteroids in co-orbital motion with Jupiter. The green and purple horizontal lines in $e = 0.7$ and $e = 0.83$ correspond to the possible crossing with the Mars' and Saturn's orbit, respectively. In particular, it can be seen a high number of asteroids in the neighborhood of the L_4 and L_5 Lagrangian equilibrium points with low eccentricities, the very well-known Trojans. But it is possible to notice also some asteroids in QS and HS motion and some TP objects with higher eccentricities.

In the following subsections, we report in detail, for each planet, some significant cases of dynamics observed.

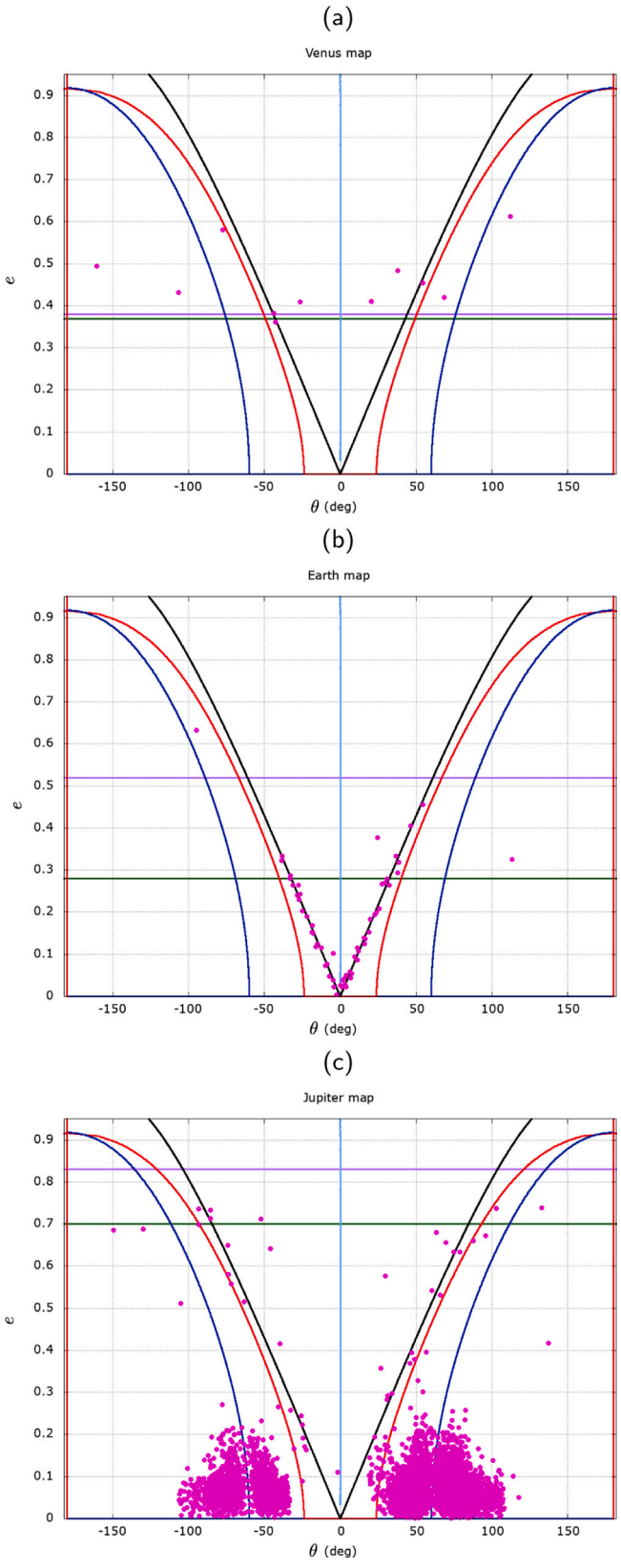

Fig. 4. The co-orbital objects found on quasi-coplanar orbits are depicted in magenta in the (θ, e)-map, considering the values of the closest co-orbital configuration with respect to the current date. (a) Venus, (b) Earth, (c) Jupiter. (For interpretation of the references to color in this figure legend, the reader is referred to the web version of this article.)

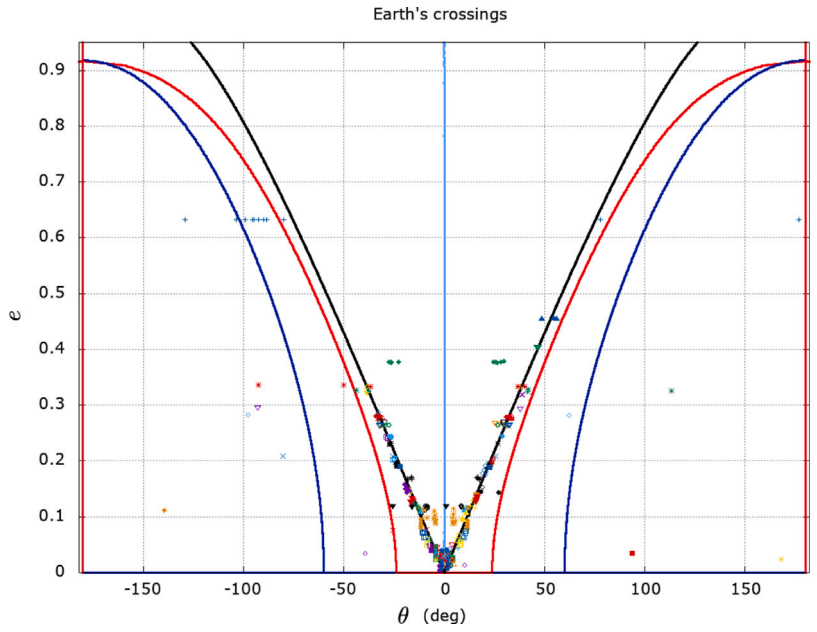

Fig. 5. Earth's (θ, e)-map is again considered. Each co-orbital object is represented with a different color and symbol. The same symbols depict different crossings in $u = 0$ of the same object in the considered time span. (For interpretation of the references to color in this figure legend, the reader is referred to the web version of this article.)

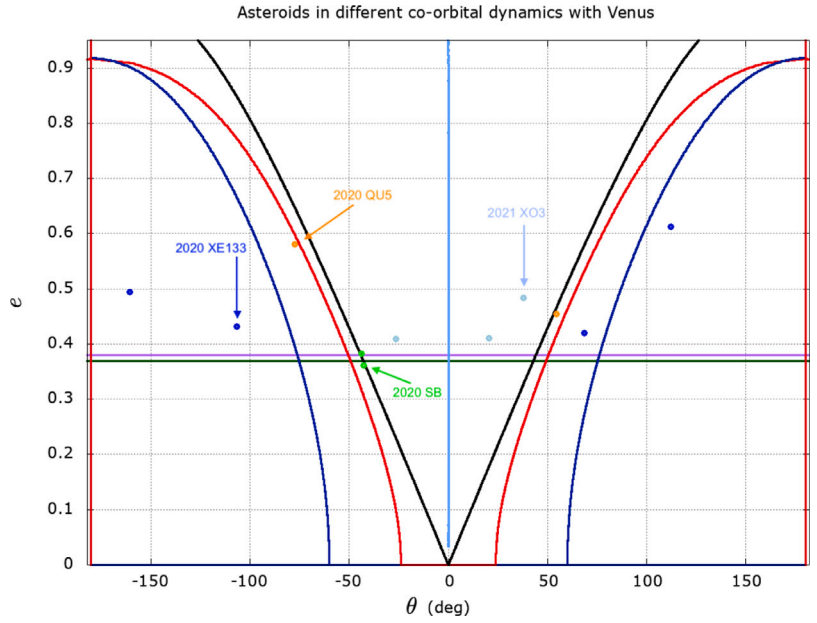

Fig. 6. Venus co-orbital objects in the (θ, e)-map are depicted at the current date and colored according to their dynamics: QS trajectories in sky blue, TP motion in blue, compounds orbits in green, transient behavior in orange. No object in a stable HS regime (with respect to the considered time frame) has been detected. The highlighted asteroids are described in detail in the following figures. (For interpretation of the references to color in this figure legend, the reader is referred to the web version of this article.)

4.1. Venus

Let us start by describing the objects in co-orbital motion with Venus. In Fig. 6, groups of asteroids have been highlighted according to their dynamics and position on the map at the current date: objects in QS dynamics are plotted in sky blue, while TP asteroids are highlighted in blue. The objects in green are in *compound* motion, that is a type of dynamics that has not been defined in Section 2, and that results from the coexistence of two types of co-orbital behaviors, QS and HS motions in these cases. An example will be given in the following. The objects in orange are instead in *transient* orbits, that is objects in a co-orbital motion that in the considered time frame changes in time, passing from a given domain to another, for instance from HS to TP, from QS to HS or vice versa. The highlighted asteroids in Fig. 6 are taken as examples of the main cases that the methodology can model or not. To this end, they will be described in detail in the following.

Fig. 7 shows the dynamics of the asteroid 2021 XO3 in QS motion. On panel (a), the colored points on the (θ, e)-map represent the crossings with the section $u = 0$ during the considered time frame. The numbers represent the chronological order of such intersections. It can be useful to compare the first panel (a) with panels (b) and (c), that show the evolution of the variable θ as a function of time t and the projection of the trajectory in the (θ, u) plane, respectively. In the three figures, the first four intersections are highlighted with a color and a number; the other intersection points are colored in sky blue, being the object in QS motion. Finally, panel (d) shows the motion of the asteroid

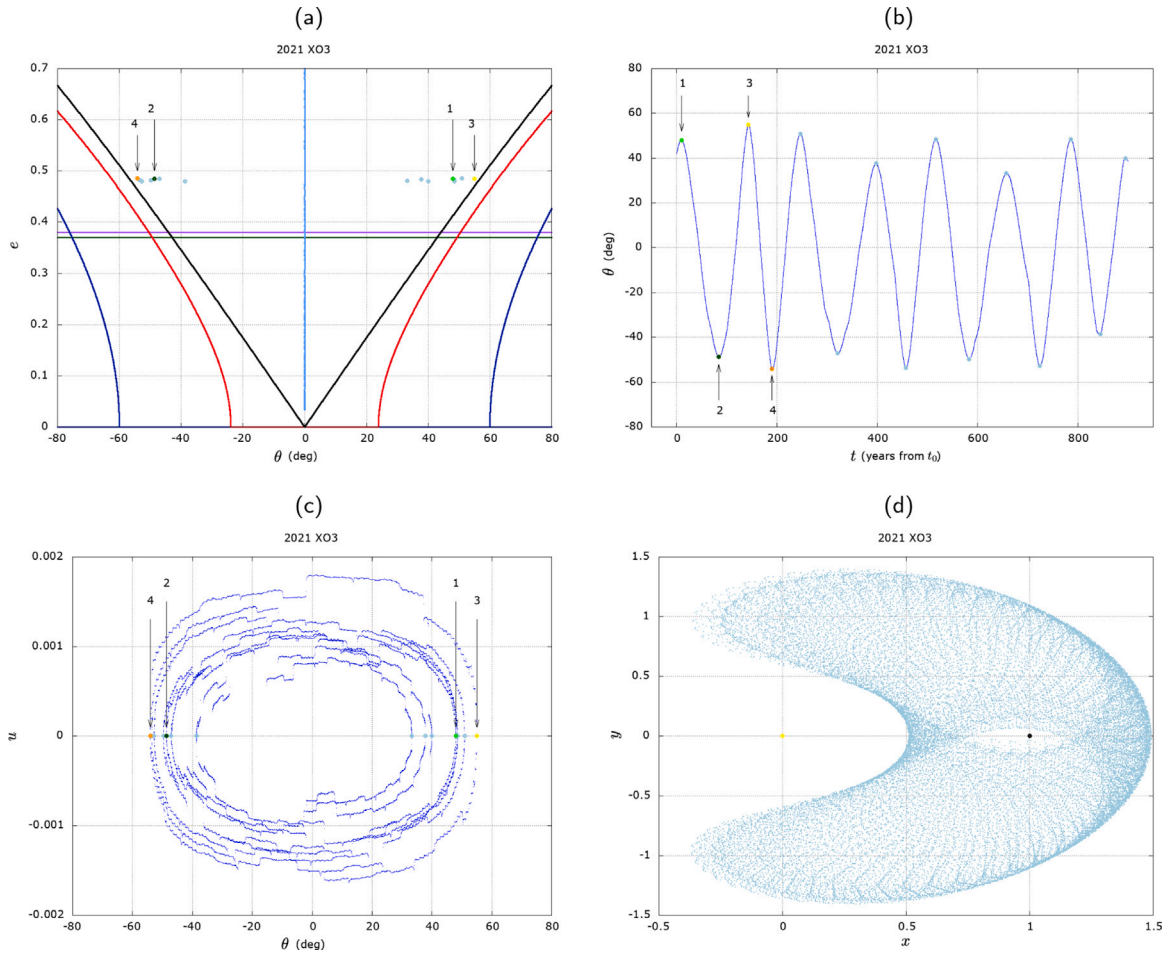

Fig. 7. Asteroid 2021 XO3 in QS motion with Venus. Panel (a): (θ, e)-map at different times. The numbers represent the chronological order of intersections $u = 0$. Panels (b) and (c): respectively, the motion of the asteroid in θ with respect time, and in the (θ, u) plane; in each of the three plots the points stand for the intersection of the asteroid with $u = 0$; the numbers correspond to the chronological order of intersections. Panel (d): the motion of the asteroid in the heliocentric synodic reference frame colored in sky blue, being in QS motion; the points $(0, 0)$ and $(1, 0)$ correspond to Sun and Venus positions, respectively. (For interpretation of the references to color in this figure legend, the reader is referred to the web version of this article.)

in the heliocentric synodic reference frame, where the Sun is located at $(0, 0)$ and Venus is at $(1, 0)$.

The asteroid 2021 XO3 has a very low inclination of about 3° with respect to the Venus orbital planet, therefore it is very close to the domain of validity of the model given by the averaged problem in the planar circular case. In the framework of the model, the crossings should take almost two values of θ on both sides of the family f with the same value of eccentricity. One can observe on panel (a) that the crossings are constant in terms of eccentricity, but, in terms of $|\theta|$, it extends in the range $[30°, 60°]$. As it is displayed on panel (b), this significant range is the results of the variations of the amplitude of libration around the origin of the (θ, u) plane. The high eccentricity of the asteroid ($e \simeq 0.5$) indicates that the orbit of the asteroid intersects the orbits of Mercury and Earth at each revolution. Hence, the perturbation of the two planets could be the reason of the observed variations in the amplitude of libration and thus in terms of θ at the crossing. Nonetheless, the information given in the (θ, e)-map is sufficient to identify the QS dynamics.

Fig. 8 shows the orbit of the asteroid 2012 XE133. It moves on a TP orbit associated with L_5, from the initial time t_0 to about $t_0 + 560$ years. After that moment, the object is thrown out from the resonance (the resonant angle θ circulates), and starts to orbit around the Sun not in resonance with Venus, although its semi-major axis remains comparable with that of Venus. It can be assumed that at that moment some external effects, such as a close approach with a planet (Mercury or Earth) can act in such a way to modify the dynamics.

Panels (a), (b), (c) represent, respectively, the crossings in the (θ, e)-map, and the projection of the orbit in the (t, θ), (θ, u) planes; as before, the first colored six points represent the six first intersections with $u = 0$ and the numbers indicate the chronological order of such intersections. The remaining points are plotted in blue as the reference color for the TP motion. This asteroid has an inclination with respect to the Venus orbital plane of about 10° and its eccentricity is high (about 0.45). As the previous case of the asteroid 2021 XO3, the oscillations of the TP motion phase reflect a sort of instability possibly due to external perturbations: in panels (a) and (c), *even* numbered intersections do not overlap each other such as the *odd* ones do, and in panel (b) the oscillations have always a different amplitude up to disappearing when the motion becomes rotational. Notice that the escape from the resonance occurs after a small, but notable diminution of the eccentricity at the crossing (Fig. 8a). The co-orbital motion can be completely deduced by the (θ, e)-map, provided that the crossing points are numbered. Finally, panel (d) shows the motion of the asteroid in the heliocentric synodic reference frame: in blue the evolution between time t_0 and t_0+560 years where the asteroids is in TP motion, while the remaining time where no resonances are present is plotted in gray.

Fig. 9 shows the motion of the asteroid 2020 QU5 which follows two types of co-orbital motion. At the beginning of the time interval

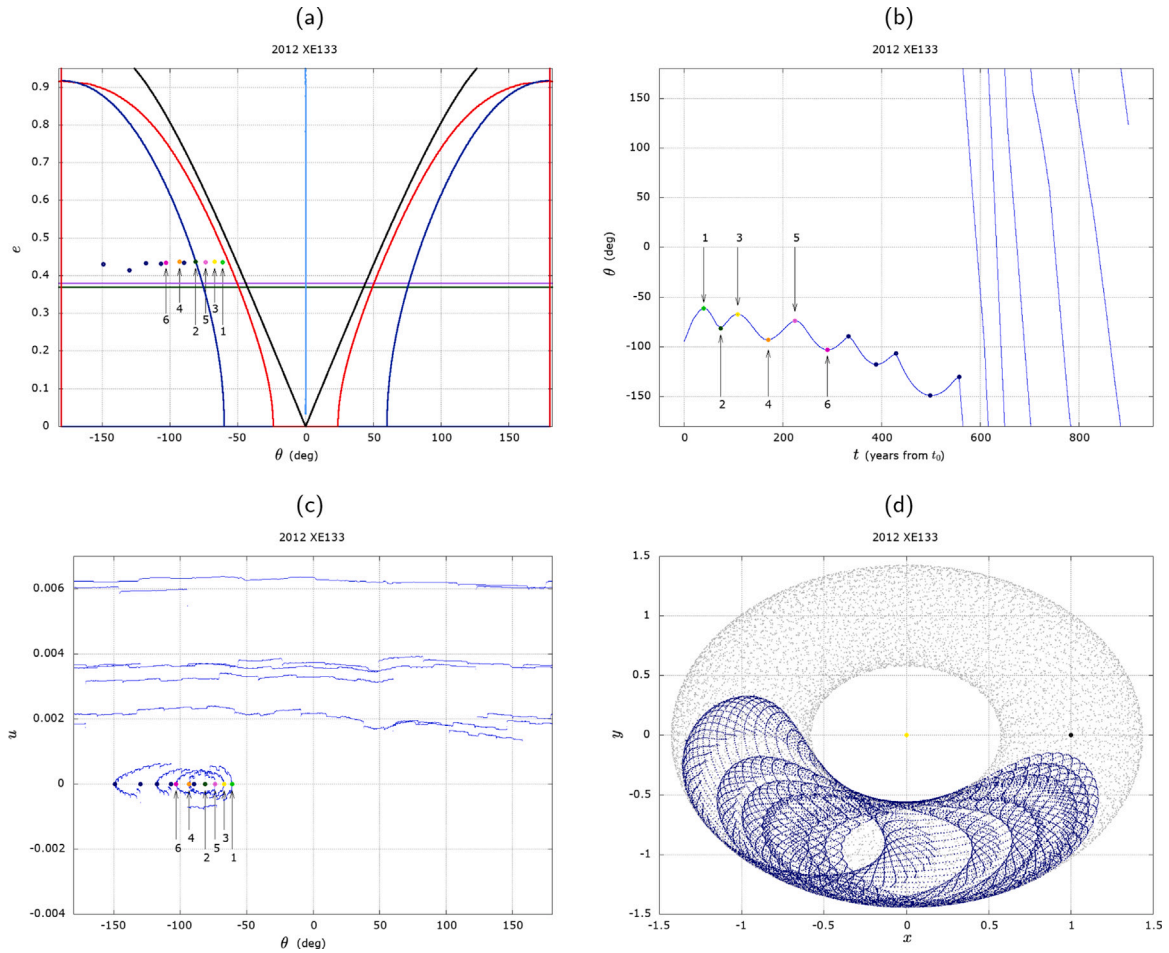

Fig. 8. Asteroid 2012 XE133 on a TP orbit of L_5 with Venus. Panel (a): (θ, e)-map at different times. The numbers represent the chronological order of intersections $u = 0$. Panels (b) and (c): respectively, the motion of the asteroid in the (t, θ) and (θ, u) planes; in each of the three plots the points stand for the crossing in $u = 0$; the numbers correspond to the chronological order of intersections. Panel (d): the motion of asteroid in the heliocentric synodic reference frame (in blue the TP motion is represented, while the interval time where the body is not in resonance with Venus is colored in gray); the points $(0, 0)$ and $(1, 0)$ correspond to the Sun and Venus positions, respectively. (For interpretation of the references to color in this figure legend, the reader is referred to the web version of this article.)

considered, it is temporarily in HS motion and after a certain time it performs a *transition* to a TP motion. As before, panels (a), (b), (c) represent, respectively, the crossings with the section $u = 0$ in the (θ, e)-map, and the projection of the trajectory in the $(t, \theta), (\theta, u)$ planes; the points represent the intersections with the plane $u = 0$; the numbers indicate the chronological order of part of such intersections. In particular, numbers 1 and 2 represent a HS dynamics, that could be visualized in all the three figures. Numbers 3 and 4 and the remaining blue points stand for the motion in TP associated with L_5. Also in this case the co-orbital motions and the transition from the HS regime to the TP one can be completely deduced by looking to the (θ, e)-map, provided that the crossing points are numbered.

In panel (d) the motion of the asteroid in the synodic reference frame is shown for the two different dynamics: before, the red motion (HS dynamics) is plotted from time t_0 up to time $t_0 + 130$ years while the blue motion (TP dynamics) is plotted from time $t_0 + 130$ up to time $t_0 + 950$ years (final time). The inclination of the asteroid with respect to the Venus orbital plane is quite low (about 2.6°), while the high eccentricity (almost 0.6) could be responsible of close encounters with Earth or Mercury which would cause the dynamics to change from HS to TP.

Fig. 10 shows a particular case of co-orbital motion for which the resonant angle θ avoids a value close to −50°. Actually, the asteroid 2020 SB is a case of 1:1 resonant motion in *compound* HS-QS dynamics (see, e.g., Christou, 2000; Brasser et al., 2004). This terminology derives from the composition of two different dynamics, – QS and HS in this case[1] – such that the resonant variables (θ, u) feature periodic oscillations and thus the trajectory moves continuously from the HS domain to the QS domain, to then turning back to the HS domain. Notice that in this case we do not speak of a transition from a given temporary type of co-orbital motion to another, but we define another orbital regime of the co-orbital resonance. Indeed, this behavior can be understood by the disappearance of one of the two lines corresponding to the singularities of collision in the phase portrait of Fig. 1, and thus it cannot occur in the framework of the planar circular case of the RTBP, where such lines bound the QS and the HS domains.

As a matter of fact, according to Sidorenko et al. (2014), the compound dynamics appears in the framework of averaged problem of the spatial circular RTBP. Being the inclination of the asteroid significant, about 9° with respect to the Venus orbital plane, this is consistent with their theory and highlights that a threshold of 10° with respect to the orbital plane may be too large in order to use the model given by the averaged problem in planar circular case. This limit should be however verified by considering a larger number of cases and in different Sun–planet systems.

In panels (b) and (d), which are enlargements of panels (a) and (c), respectively, and in panel (e), five points representing the intersections with $u = 0$ are shown and they are numbered in chronological order.

[1] In the spatial case of the RTBP, other types of compound have been described, such as TP-QS or TP-QS-TP (see, e.g., Christou, 2000).

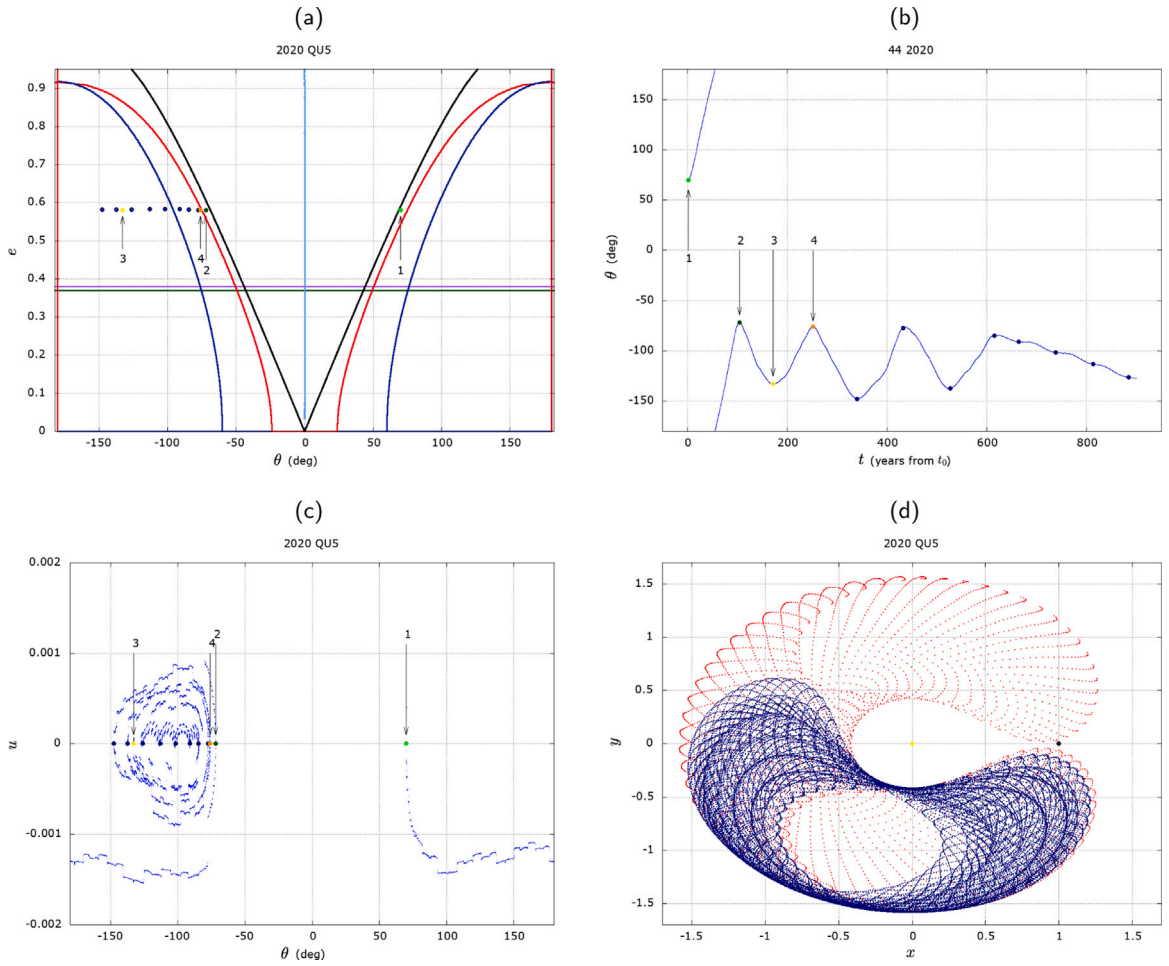

Fig. 9. Asteroid 2020 QU5 in a co-orbital transient dynamics with Venus. Panels (a), (b), (c) represent, respectively, the crossings with the section $u = 0$ in the (θ, e)-map, and the projection of the trajectory in the $(t, \theta), (\theta, u)$ planes; the points represent the intersections with $u = 0$; the numbers indicate the chronological order of part of such intersections. Panel (d) shows the motion of asteroid in the synodic reference frame (in red the HS dynamics and in blue the TP motion); the points $(0, 0)$ and $(1, 0)$ correspond to the Sun and Venus positions, respectively. (For interpretation of the references to color in this figure legend, the reader is referred to the web version of this article.)

Odd numbers represent the crossings of the trajectory in the HS domain, while even numbers a crossing in the QS region. Panel (b) clearly shows that in the (θ, e)-map the intersections with $u = 0$ cross the collision curve, and thus they belong alternatively to one of the two domains. In this panel, following the numbered crossing points we can perfectly derive the nature of the compound motion. Finally, in panel (f) the motion of the asteroid in the synodic reference frame is shown for two different part of the compound dynamics: the red motion, standing for the HS part of the dynamics, is plotted from time t_0 up to time $t_0 + 209$ years and the sky blue motion, standing for the QS part of the dynamics, takes place from time $t_0 + 209$ up to time $t_0 + 286$ years. Notice that in the analysis performed a significant number of objects appear to follow in compound HS-QS motion, especially for the Earth (see next section), and this is one of the reasons why in the near future we aim at analyzing the three-dimensional case for a more complete treatment of this dynamics.

We can conclude that, in the four examples shown for Venus, the information given by the (θ, e)-map fits perfectly with the type of co-orbital motion of the given asteroid.

In Table 3, we give the list of the asteroids in co-orbital motion with Venus following the JPL Horizons ephemerides. The data correspond to the intersection with the section $u = 0$, that occurs at the closest epoch with respect to the reference epoch. The last column indicates the type of co-orbital motion detected in the given time frame.

Table 3
The co-orbital objects found for the Sun–Venus system on quasi-coplanar orbits. The values reported refer to the intersection with $u = 0$, that is the closest one to the current date, assumed to be 2021-03-21 00.00.00 (JD 2459294.50). The angular values are reported in degrees and are defined with respect to the orbital plane of the planet. The last column indicates the co-orbital dynamics detected in the given time frame (CP refers to compound, TR to transient). These co-orbital configurations are shown also in Fig. 4a and Fig. 6.

Asteroid	t (JD)	a (au)	e	I	θ	Dynamics
2001 CK32	2463638.72	0.72333158	0.382	5.68	−43.834	CP
2002 LT24	2375731.02	0.72307523	0.494	3.84	−160.581	TP
2002 VE68	2475698.55	0.72333068	0.409	12.33	−26.292	QS
2012 XE133	2462143.09	0.72421895	0.432	10.03	−106.692	TP
2013 ND15	2454656.87	0.72343445	0.612	1.95	111.984	TP
2020 BT2	2462807.58	0.72333585	0.420	5.40	68.586	TP
2020 QU5	2463543.58	0.72333067	0.581	2.61	−77.507	TR
2020 SB	2453862.11	0.72338904	0.362	8.80	−42.723	CP
2021 XA1	2465246.93	0.72333198	0.410	3.02	20.629	QS
2021 XO3	2450832.85	0.72363671	0.484	2.82	37.760	QS
2022 AP1	2509314.03	0.72252306	0.455	1.52	54.384	TR

4.2. Earth

Let us continue the analysis focusing on two examples of co-orbital motion in the Sun–Earth system.

Fig. 11 shows the HS dynamics of the asteroid 2019 VL5. Differently from the previous cases analyzed for Venus, here, a greater regularity

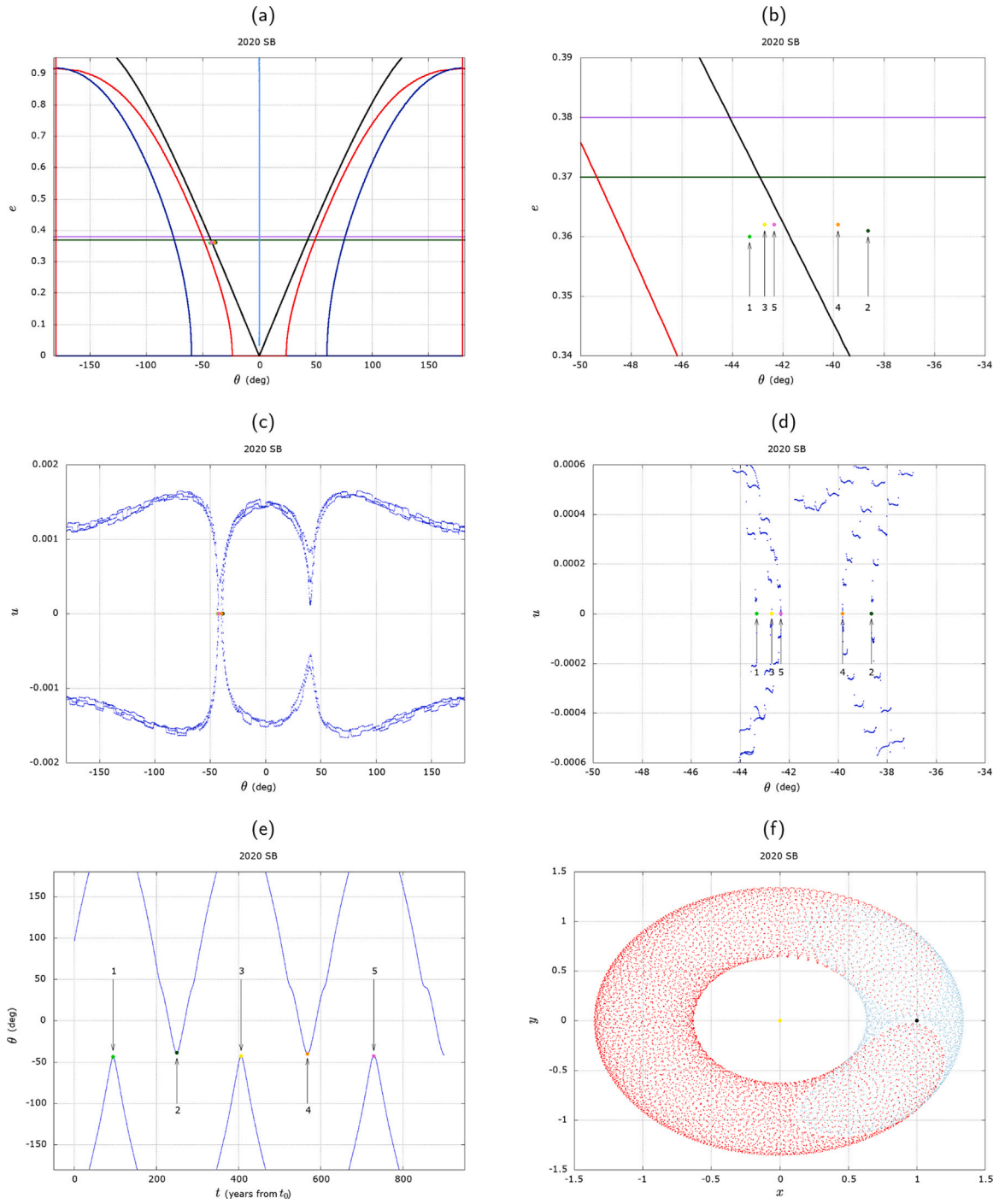

Fig. 10. Asteroid 2020 SB whose orbit features a compound HS-QS motion. Panels (a), (c), (e) represent, respectively, the crossings of the section $u = 0$ in the (θ, e)-map, and the projection of the trajectory in the $(t, \theta), (\theta, u)$ planes; the points stand for the crossings; panels (b), (d) are enlargement of panel (a), (c), respectively; the numbers correspond to the chronological order of crossings. Panel (f) shows the motion of asteroid in the synodic reference frame; the points $(0, 0)$ and $(1, 0)$ correspond to the Sun and Venus positions, respectively.

in the dynamics is observed: in the considered time span the asteroid moves in the (t, θ) plane (panel (b)) with regular oscillations with a same amplitude and in panels (a) and (c) the different points referring to the intersection with $u = 0$ overlap perfectly. The inclination of such asteroid is 1° with respect to the Earth's orbital plane, so that the averaged problem in the planar approximation is adequate in this case. Moreover, the eccentricity of the orbit of this asteroid (about 0.279) is such that its orbit is close to the intersection with the orbit of Venus. It can be argued that this configuration locks the regular motion of the asteroid. Finally, panel (d) shows the motion of asteroid in the synodic reference frame for the whole interval time.

In this case, although very close to the separatrix, the points representing the crossings with the section $u = 0$ in the (θ, e)-map (panel (a)), lie in the region of the phase space relative to the horseshoe dynamics. Thus, the information given in the map can identify properly the dynamics of interest. Moreover, this example is in agreement with the recent Qi and Qiao (2022), where the asteroid is found to be in a

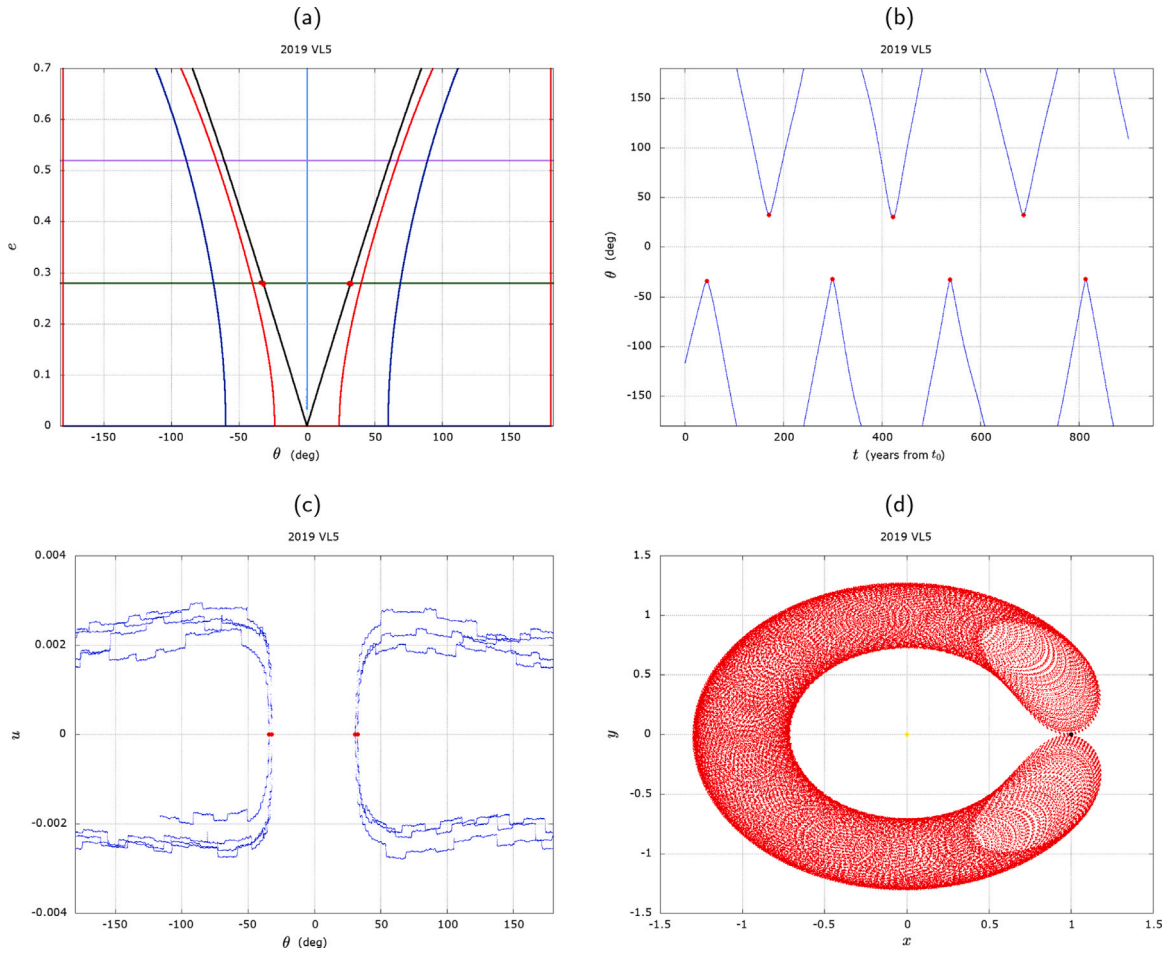

Fig. 11. Asteroid 2019 VL5 in HS dynamics with the Earth. Panels (a), (b), (c) show, respectively, the crossings with the section $u = 0$ in the (θ, e)-map, and the projection of the trajectory in the (t, θ), (θ, u) planes; the red dots represent the intersections with $u = 0$; panel (d) shows the motion of asteroid in the synodic reference frame; the points $(0, 0)$ and $(1, 0)$ correspond to the Sun and Earth positions, respectively. (For interpretation of the references to color in this figure legend, the reader is referred to the web version of this article.)

QS-HS state for at least 3000 years and its current state is HS for at least 800 years.

Fig. 12 analyzes the motion of the well-known asteroid 2016 HO3, named Kamo'oalewa. At the current date, it turns out to follow a QS dynamics, but, as it can be inferred from the figures, this dynamics is temporary: its orbit will switch to the HS regime in the future, in the same way it did in the past, going from the HS to the QS regime. In other words, as in the case of asteroid 2020 QU5 for Venus, the asteroid has a transient behavior. Observing panel (b), which is an enlargement of the (θ, e)-map represented in panel (a), all the dots corresponding to the intersections with $u = 0$ belong to the QS domain although some of them, namely the ones numbered 1 and 2 and the not-numbered red dots lie in the HS realm. This means that, in this case, observing the (θ, e)-map we cannot obtain a correct information. We can only deduce the QS-HS state by comparing panel (a) with panel (e), where the variation of θ with respect the time t is represented. The dots numbered 2 and 4 and all the other sky blue dots belong instead to the QS dynamics, following the (θ, e)-map issued from the planar circular model. We conclude that due to the non-negligible inclination of the orbit of this asteroid (about 9° with respect to the Earth's orbital plane), the planar model is not entirely satisfactory to describe the dynamics, especially close to the boundary associated with the collision curve, and a three-dimensional model is needed to explain this kind of motion. In panels (b), (d), (e) the four numbered dots stand for the first four intersections $u = 0$ in chronological order. Panel (f) shows the motion of asteroid in the synodic reference frame and in particular the red part represents the HS motion between time t_0 and time $t_0 + 317$ years and the sky blue represents the QS motion between time $t_0 + 317$ and time $t_0 + 720$ years.

In Table 4, the list of the co-orbital objects on quasi-coplanar orbits with the Earth is given. The objects correspond to the data depicted in Fig. 4b. The last column of the Table indicates the detected co-orbital dynamics. It refers to the dynamics in the whole time span, except for the cases where the asteroid escapes from the co-orbital regime or if it experiences a too close approach with the Earth and thus the ephemerides are not reliable. In these cases we report the closest dynamics to what is considered as the current date.

Note that to be able to identify the objects in co-orbital motion with the Earth at a given epoch as a function to their heliocentric orbital elements is of particular relevance both for planetary science and space engineering purposes. Indeed, asteroids that can orbit in the neighborhood of the Earth are not necessarily a threat for the Earth, but they can represent unique opportunities for science and resource retrieval. In this regards, the map in Fig. 4b, can be enriched by adding the information on the minimum distance to the Earth (Pousse and Alessi, 2022), the corresponding Jacobi constant (Pousse and Alessi, 2021), the fundamental frequencies of the quasi-periodic approximation of the co-orbital trajectory, or the taxonomy of asteroids (e.g., C-type), if known. The map depicted shows the co-orbital configuration at a date that is not necessarily in the future, following the approach of this study, but a different choice can be made. In this way, the map can represent a valuable tool in the preliminary phases of the mission analysis.

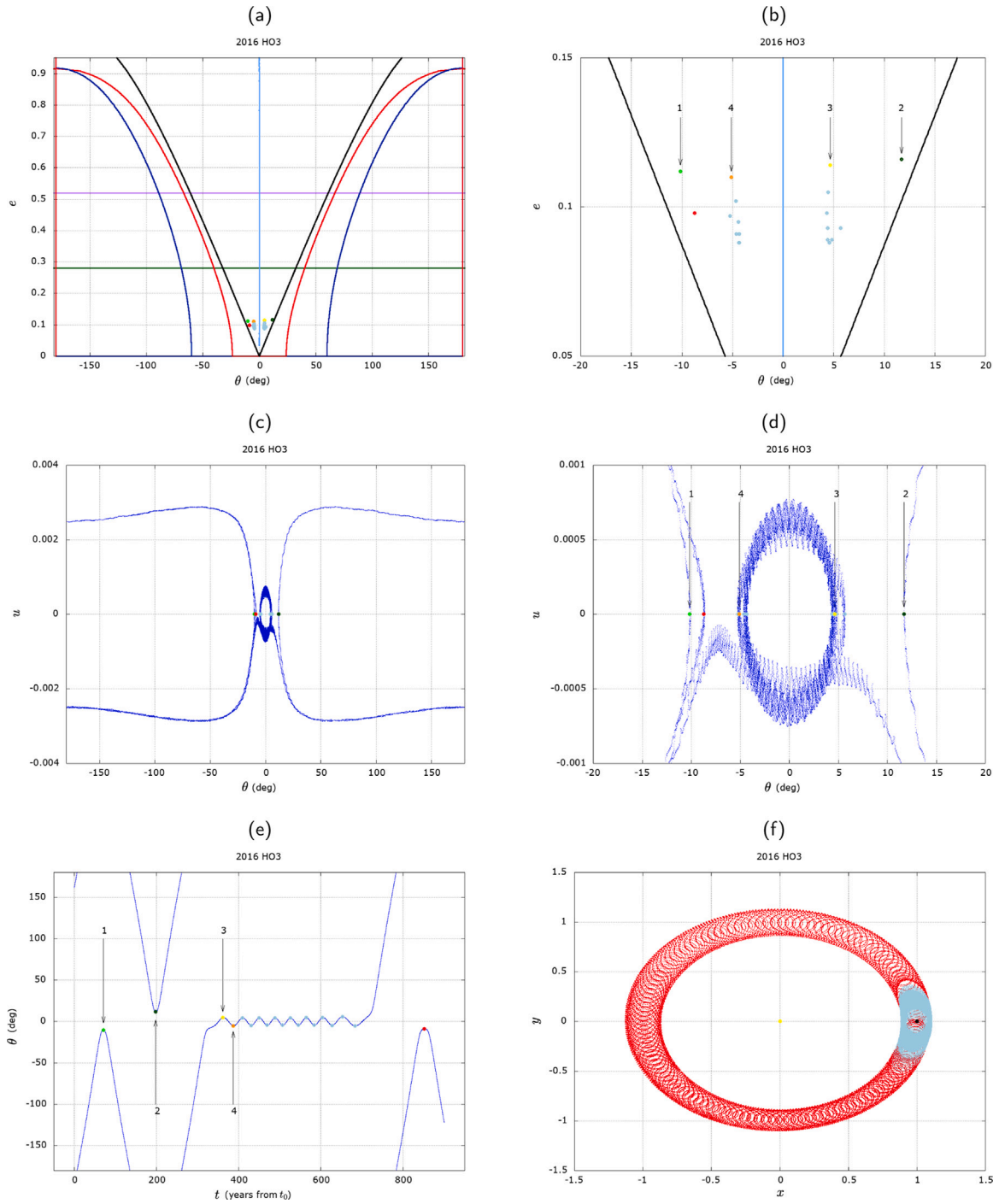

Fig. 12. The transient behavior of the asteroid 2016 HO3 with the Earth. Panels (a), (b), (c) show, respectively, the crossings with the section $u = 0$ in the (θ, e)-map, and the projection of the trajectory in the (t, θ), (θ, u) planes; the colored points represent the intersections with $u = 0$; panels (b), (d) are enlargements of panels (a), (c), respectively; panel (f) shows the motion of asteroid in the synodic reference frame; the points $(0, 0)$ and $(1, 0)$ correspond to the Sun and Earth positions, respectively. (For interpretation of the references to color in this figure legend, the reader is referred to the web version of this article.)

4.3. Jupiter

As very well known and also evident from Fig. 4c, Jupiter has a large number of asteroid orbiting in 1:1 mean-motion resonance with it.[2] The peculiarity of the case of Jupiter lies in the *regularity* of the motions of such objects. In this case the JPL Horizons ephemerides covers a time span of 600 years. Four cases are analyzed here: the first three are chosen in order to show such regularity which is not present in the cases of Venus and Earth.

Fig. 13 shows the asteroid 2015 BB555 in a QS dynamics. Although the eccentricity and inclination of the orbit of this body are high, 0.68 and 10° (with respect to the Jupiter orbital plane), respectively, panels (a), (b) and (c) show that the amplitudes of oscillations of θ are regular for the whole interval of time. These figures can be compared with the case of a QS dynamics found for Venus, the one shown in Fig. 7 where each oscillation in the (t, θ) plane is different from the others, due

[2] 7883 at the L_4 point and 4097 at the L_5 point on 2022 July 26 (Minor Planet Center, 2022).

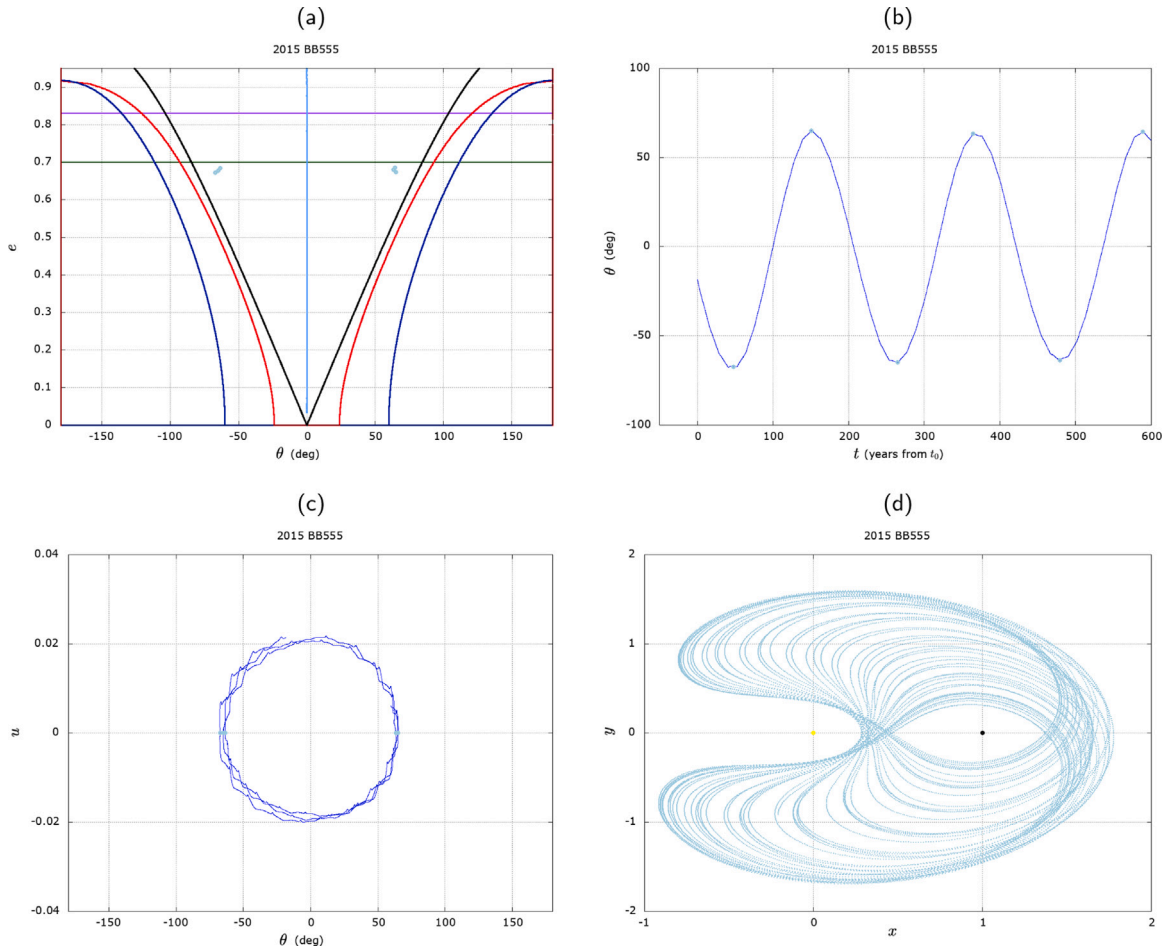

Fig. 13. Asteroid 2015 BB555 in QS motion with Jupiter. Panels (a), (b), (c) show, respectively, the crossings with the section $u = 0$ in the (θ, e)-map, and the projection of the trajectory in the (t, θ), (θ, u) planes; the sky blue dots represent the intersections with the plane $u = 0$; panel (d) shows the motion of asteroid in the synodic reference frame; the points $(0, 0)$ and $(1, 0)$ correspond to the Sun and Jupiter positions, respectively. (For interpretation of the references to color in this figure legend, the reader is referred to the web version of this article.)

probably to external perturbations (as, for example, close encounters with Earth or Mercury).

The same analysis can be done for the asteroid 2014 ED239, as shown in Fig. 14. In this case, the orbit follows a HS dynamics, characterized by a small eccentricity (less than 0.08) and a high inclination (about 12°). In the considered time span the asteroid remains trapped in its dynamics. Nevertheless, it is expected that after a certain amount of time, the asteroid will switch to another dynamics or escape from the co-orbital resonance. Indeed, according to the numerical simulations of Ćuk et al. (2012), all the HS orbits become unstable if the mass of the third body is at least about one Jupiter mass.

Even more striking is the case of the Trojan 2014 CL35, shown in Fig. 15. With its quite small eccentricity (about 0.05) and quite high inclination (about 7°), this asteroid looks like to be in a perfect TP motion associated with L_4. In panel (c) the intersection points with $u = 0$ coincide perfectly. As panel (a) shows, only the eccentricity at the crossing experiences small variations, that are probably due the eccentricity-inclination exchanges generated by the Lidov-Kozai-type first integral that exists in the framework of the averaged problem of the 1:1 mean-motion resonance in spatial circular case (see, e.g., Pousse and Alessi, 2022).

The last case of Jupiter has some other peculiarities. In Fig. 16, the orbit of the asteroid 2014 EC59 performs many transitions in the considered time span: it begins to be in an HS dynamics and then moves into a TP orbit associated with L_5, then moves back to a HS dynamics and again into a TP orbit associated with L_4. Although the orbit is characterized by a quite high inclination (more than 7°) and a moderate eccentricity (about 0.2), the (θ, e)-map shown in panel (a) fits quite well with the model. The numbers indicate the chronological order of the $u = 0$ intersections and it is possible to notice that number 1 is in the HS domain, number 2 is in the L_5 TP domain, again number 3 and 4 are in the HS domain and, finally, number 5 is in the L_4 TP domain. The same is well represented with the same numbers in panels (b) and (c). Panel (d) is split in four time intervals: the first is from $t_0 = 0$ to $t_0 + 75$ years and the third is from $t_0 + 200$ years to $t_0 + 460$ and they are plotted in red representing the HS motion; the second is from $t_0 + 75$ years to $t_0 + 200$ years and the fourth is from $t_0 + 460$ years to $t_0 + 600$ and they are plotted in blue representing TP motion of L_5 the former and TP motion of L_4 the latter.

In all the examples presented for Jupiter, although each of them with its own peculiarity, the information given by (θ, e)-map is sufficient to characterize the dynamics (also in case of transition).

The maps of Fig. 4 represent a snapshot of the co-orbital population at a given epoch. To represent the evolution of a single object, the points on the (θ, e)-map have to be associated to the numbered order of the crossings, to deduce the dynamics in an unequivocal way. This is especially important in the case of transitions and compound motion, because only in this way we can distinguish between the two. For a compound motion, the asteroid will alternate from one regime to the other; for a transition, it will be associated to the same domain continuously for a number of times.

In Table 5, the objects in the Sun–Jupiter system that in the given time span follow a co-orbital motion, that is not a regular TP orbit,

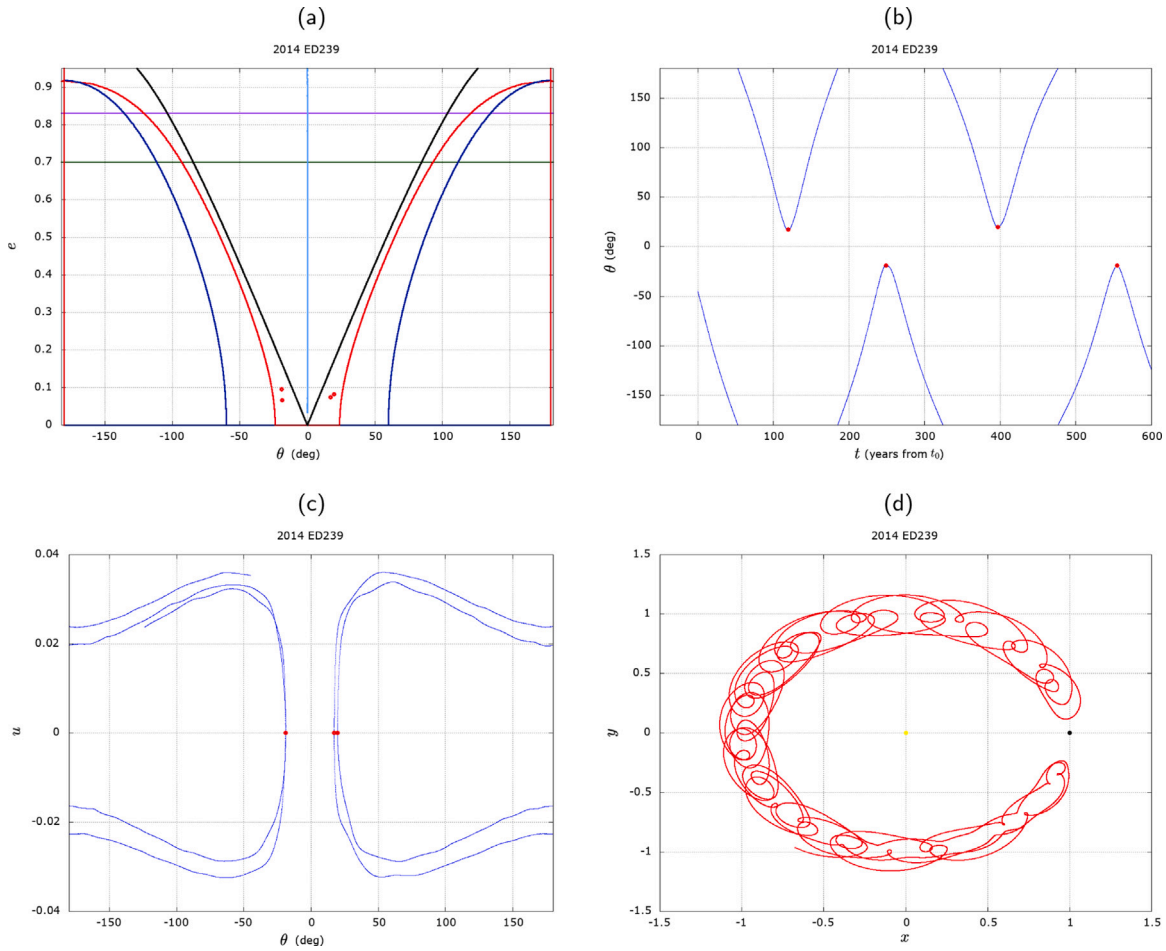

Fig. 14. Asteroid 2014 ED239 in HS motion with Jupiter. Panels (a), (b), (c) show, respectively, the crossings with the section $u = 0$ in the (θ, e)-map, and the projection of the trajectory in the (t, θ), (θ, u) planes; the red dots represent the intersections with the plane $u = 0$; panel (d) shows the motion of asteroid in the synodic reference frame; the points $(0, 0)$ and $(1, 0)$ correspond to the Sun and Jupiter positions, respectively. (For interpretation of the references to color in this figure legend, the reader is referred to the web version of this article.)

are listed. In other words, only the asteroids in QS, HS, compound or transition regime (under the quasi-coplanar approximation) are given.

Finally, the list of the objects, that following the algorithm explained in Section 3 can be considered Trojans, have been compared with the ones given by the Minor Planet Center (2022), in the considered inclination range. It turns out that the objects 2000 QV233, 2009 WF218, 2014 ES72, 2014 EY243 are co-orbitals according to the analysis presented here but not properly in a TP motion, while the MPC considers them as Trojans. On the other hand, the MPC's list does not contain the following asteroids, that according to our analysis are Trojans, 2008 YL115, 2014 ES70, 2014 EL76, 2014 EJ135, 2014 EJ169, 2014 EL244, 2014 RV60, 2015 HF178, 2015 YB2, 2016 UP208, 2016 UN244, 2017 SF121. Notice that among these objects, 2014 ES70, 2014 EL76, 2014 EJ135, 2014 EJ169, 2014 EL244 are instead listed as Trojans by the NASA JPL SSD Small-Body Database (2022). These discrepancies will be addressed in the future.

4.4. General remarks from the analysis of the whole dataset

From the examples shown it might seem that the (θ, e)-map is not effective at identifying transitions between QS and HS motion (the case of asteroid 2016 HO3), while well identifying other transition and compound motions. From an accurate analysis of all the asteroids listed in Tables 3, 4, 5, it is important to remark the following.

- Transitions and compound motions can be identified in the (θ, e)-map only if we represent all the crossing points associated to the intersection $u = 0$ and if we number such points. As Fig. 4 depicts the co-orbital motion at one single crossing, it cannot show transitions and compound dynamics, that by definition involve an evolution of the co-orbital dynamics. Fig. 5 represents the crossings at different times for the Earth's co-orbital objects (each object with a different color): it is possible to understand if a single object remains in a same dynamics or moves from one to another, but to have a complete information it is necessary to number the order of the crossings.
- In the case of Venus, all the compound motions and transitions between different co-orbital regimes are well identified in the (θ, e)-map regardless of the eccentricity and the inclination of the asteroid.
- From Tables 4, 5 we can see that, in the time span of 900 years, much more transitions and compound motions appear in the case of the Earth with respect to the Jupiter case. We can suppose that, in a medium-term timescale, Jupiter co-orbital asteroids are more stable than Earth ones. In this regard, with "stable" we mean both staying in the same dynamical regime and a not significant change in the amplitude of oscillations of the angle θ (as shown in the examples).
- In the case of the Earth, we cannot draw firm conclusions on the accuracy of the map in depicting transition and compound dynamics. In general, we have encountered important issues in the following situations: first, when the inclinations of the asteroid is too high (although there are cases where it works well even

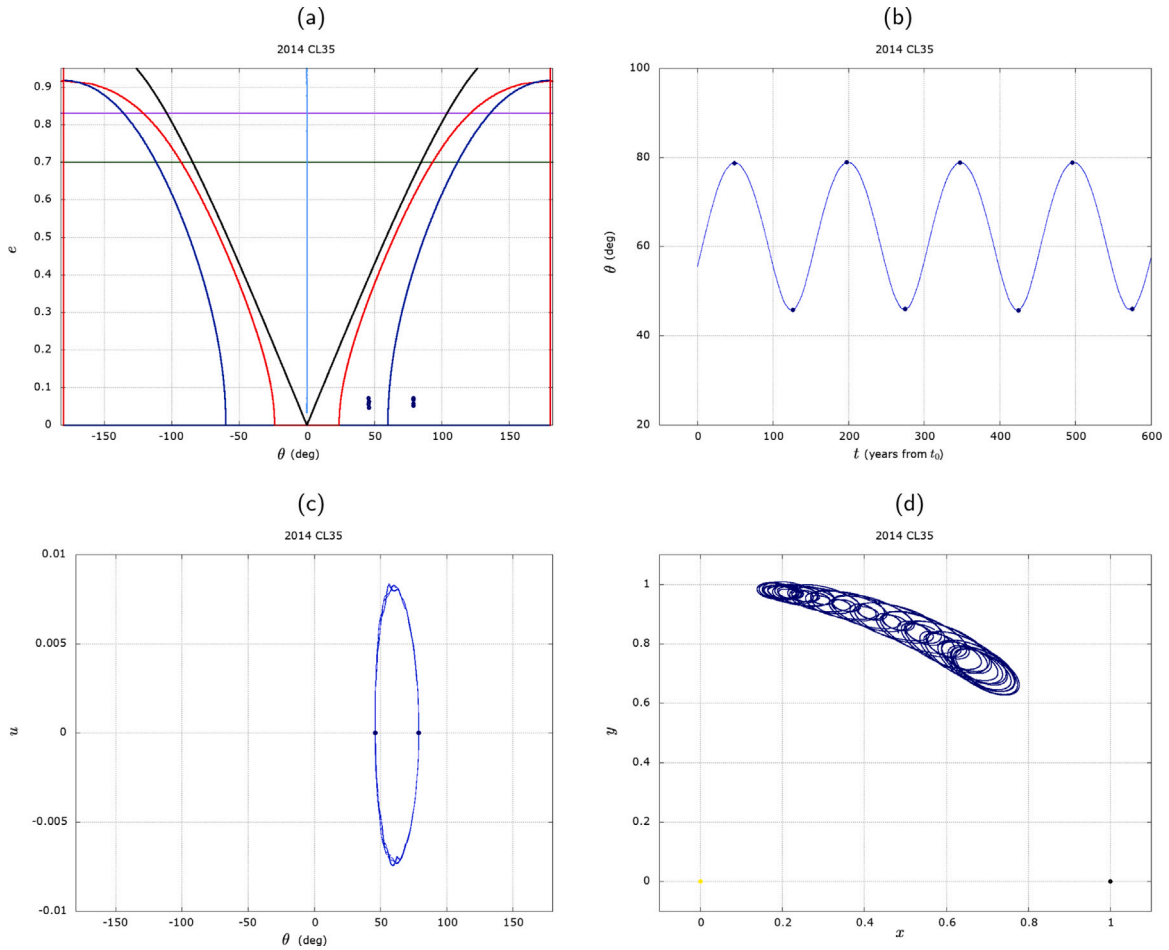

Fig. 15. Asteroid 2014 CL35 in TP motion of L_4 with Jupiter. Panels (a), (b), (c) show, respectively, the crossings with the section $u = 0$ in the (θ, e)-map, and the projection of the trajectory in the (t, θ), (θ, u) planes; the blue dots represent the intersections with $u = 0$; panel (d) shows the motion of asteroid in the synodic reference frame; the points $(0, 0)$ and $(1, 0)$ correspond to the Sun and Jupiter positions, respectively. (For interpretation of the references to color in this figure legend, the reader is referred to the web version of this article.)

for high inclinations), so in these cases it is desirable a three-dimensional model; second, when the eccentricity of the asteroid can allow a relatively close approach with Venus or Mars: in this case we expect that the map does not fit because of the perturbation due to another planet; third, when the eccentricity of the asteroid is very small (of the order of 10^{-3}). All the three cases will be investigated in future works.

– In the case of Jupiter, most of the asteroids in transition or compound regime are well identified in the map even if they are characterized by a high inclination, so we suppose that for this planet the threshold in the inclination of the orbit of the asteroid to be considered co-planar can be higher than for the Earth.

A rigorous explanation of the reasons why some cases are not well identified in the map will be addressed in the future, to figure out whether it is due to the planar approximation, to the averaged model or to an effect that is not included in the circular restricted three-body problem.

5. Conclusions and future directions

This work has focused on the medium-term ephemerides of the asteroids computed by the JPL Horizons system to look for those objects that move on a co-orbital configuration. The time frame constraints of the given ephemerides, as well as the expected period of the resonant behavior, led to limit the investigation to the Sun–Venus, Sun–Earth and Sun–Jupiter systems.

The analysis of the real data has aimed at a possible application of the integrable model given by the averaged problem of the RTBP in planar circular case, for which the different types of co-orbital motion are neatly defined. In this framework, the type of orbital regime can be identified by a simple two-dimensional map that has the remarkable feature to be independent on the mass ratio of the system, as long as this can be considered as a small parameter. Being this condition fulfilled for all Sun–planet systems of the solar system, once the tool was computed (i.e., crossings of the separatrices, collision curve and equilibrium points) then it has been applied equally for the co-orbitals of Venus, Earth and Jupiter.

In order to be close to the limit of validity of the model, the data has been restricted in inclination with respect to the orbital plane of the given planet, to what we called the “quasi-coplanar” orbits.

The procedure developed has allowed to highlight, represent in a concise way, and classify the co-orbital objects of the solar system in terms of their dynamics, whether being stable or temporary in the considered time frame. According to the study of the trajectories in the resonant variables as well as in the synodic reference frame, the results show that under some assumptions of low inclination with respect to the Sun–planet reference system the bounds of each domain of motion defined by the map fit very well with the observed behavior.

An improvement of the condition of quasi-coplanarity is necessary in order to apply the method in a systematic way. The compound dynamics, that do not exist in the framework of the planar circular case, could be a possible future research focus in order to refine the criteria, for instance through the investigation of the phase space of

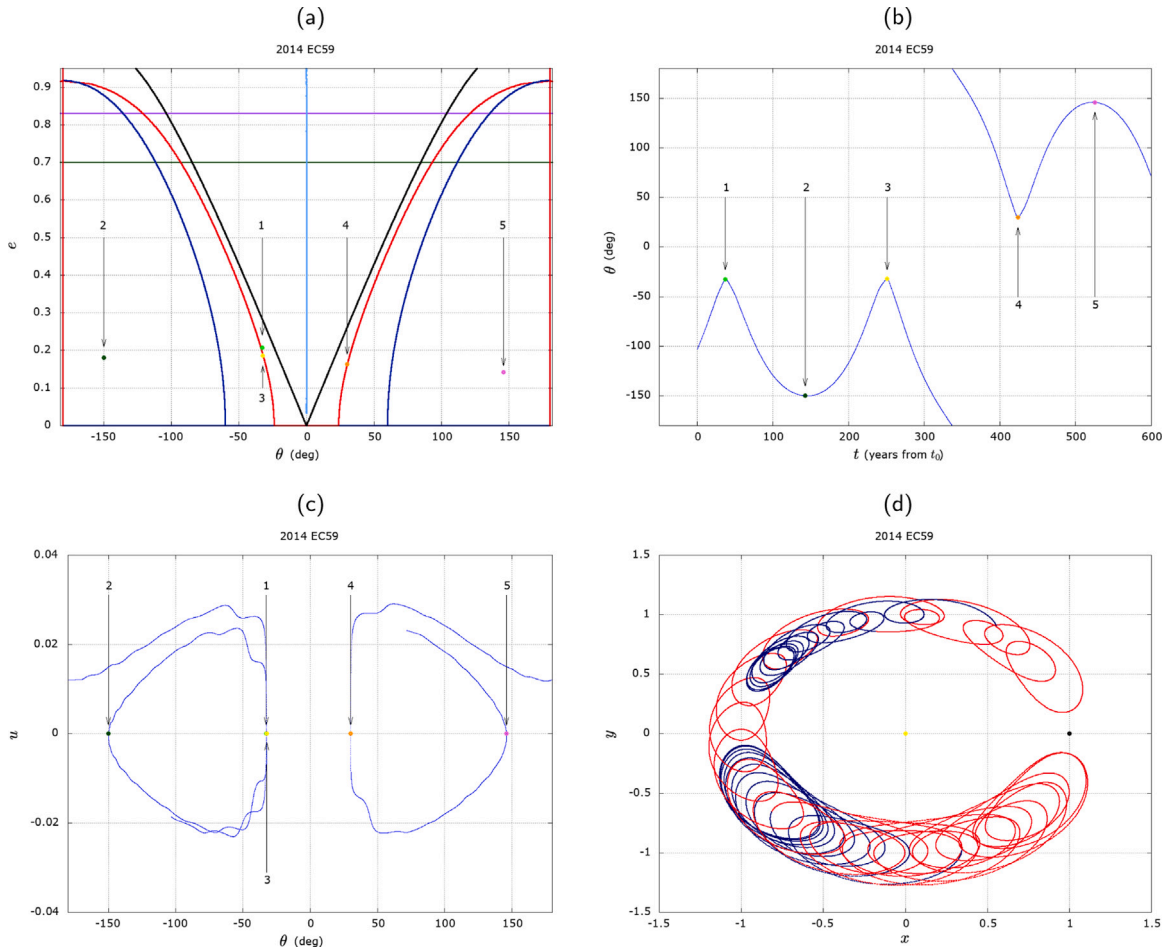

Fig. 16. Asteroid 2014 EC59 in a transient dynamics from HS to TP motion with Jupiter. Panels (a), (b), (c) represent, respectively, the motion in the (θ, e), (t, θ), (θ, u) planes; the colored dots represent the intersections with $u = 0$; panel (d) shows the motion of asteroid in the synodic reference frame; the points $(0, 0)$ and $(1, 0)$ correspond to the Sun and Jupiter positions, respectively. (For interpretation of the references to color in this figure legend, the reader is referred to the web version of this article.)

the averaged problem in the spatial circular case, to show the possible existence of a hyperbolic structure that divides the horseshoe, quasi-satellite and compound domains.

Another advantage of the map is that it allows to follow the transitions that are generated by different perturbations, namely, effects that are not included in the averaged approximation of the RTBP and effects that are external to the RTBP itself. In principle, the distinction can be drawn looking to the evolution of the Jacobi constant. As a matter of fact, in the same map its value can be depicted as shown in Pousse and Alessi (2021). If the data exhibit a significant jump in this regard, then we can conclude that the transition is due to an external perturbation associated with a different planet. A milder variation in the Jacobi constant can be provided by other effects, like the orbital eccentricity of the given planet. These aspects will be tackled in the future with the three-dimensional analysis.

Moreover, the map can be enriched also with information on the minimum distance to the considered planet, the crossing with the orbit of another planet, or the evolution of the fundamental frequencies in the different orbital regimes. In other words, a cartography of the co-orbital resonance could be drawn for each planet of the solar system in order to identify phenomena that can generate instabilities, transitions or escapes from the co-orbital resonance.

Finally, another long-term research focus is to remove the constraints in inclination in order to obtain a systematic method of detection and classification of the co-orbital objects in the solar system. To this end, a first step would be a complete exploration of the phase space of the averaged problem in spatial circular case, (4-dimensional and not integrable), and the identification of the invariant structures that may help to define the dynamics and characterize their domains in the phase space.

CRediT authorship contribution statement

Sara Di Ruzza: Conceptualization, Methodology, Visualization, Analysis of the results, Writing. **Alexandre Pousse:** Conceptualization, Methodology, Visualization, Analysis of the results, Writing. **Elisa Maria Alessi:** Conceptualization, Methodology, Software, Visualization, Analysis of the results, Writing.

Data availability

Data will be made available on request.

Acknowledgments

The authors are indebted to Tommaso Del Viscio from IMATI-CNR for the support he provided for the data processing and to Federica Spoto from CFA Harvard for the suggestions on the data retrieval.

The authors are grateful to the reviewers who helped to improve the quality of the paper.

A.P. and E.M.A. acknowledge the support received by the project entitle "*co-orbital motion and three-body regimes in the solar system*", funded by Fondazione Cariplo through the program "*Promozione dell'attrattività e competitività dei ricercatori su strumenti dell'European Research Council – Sottomisura rafforzamento*".

Table 4
The co-orbital objects found for the Sun–Earth system on the quasi-coplanar orbits. The values reported refer to the intersection with $u = 0$, that is the closest one to the current date, assumed to be 2021-03-21 00.00.00 (JD 2459294.50). The angular values are reported in degrees and are defined with respect to the orbital plane of the planet. The last column indicates the co-orbital dynamics detected in the given time frame (CP refers to compound, TR to transient). These co-orbital configurations are shown also in Fig. 4b.

Asteroid	t (JD)	a (au)	e	I	θ	Dynamics
2000 PH5	2452475.70	1.00000011	0.230	1.95	−27.004	HS
2000 EE104	2506798.05	1.00000011	0.293	5.10	37.777	HS
2005 UH6	2445884.10	1.00000015	0.632	2.66	−94.658	TR
2005 WK4	2545271.43	1.00000046	0.241	9.89	−28.449	CP
2006 FV35	2447416.15	1.00000011	0.378	7.11	24.537	QS
2016 HO3	2462506.43	1.00000011	0.102	7.81	−4.655	QS+TR
2001 GO2	2452001.06	1.00000013	0.169	4.67	−18.422	TR
2002 VX91	2395963.64	1.00000614	0.203	2.14	−24.799	CP+HS
2003 YN107	2451752.57	1.00000011	0.038	4.29	1.690	HS
2007 DD	2511123.48	1.00000031	0.115	2.95	−12.457	HS
2008 NP3	2407551.36	1.00000012	0.334	1.47	36.868	TR
2009 HE60	2454205.02	1.00000011	0.265	1.52	−27.494	TR
2009 SH2	2455111.84	1.00000021	0.094	6.85	9.359	HS+CP
2010 CK19	2455245.57	1.00004886	0.153	2.24	18.978	HS
2010 VQ98	2512982.25	1.00000012	0.026	1.92	0.244	CP
2012 BK14	2595835.56	1.00000188	0.190	1.79	−21.859	HS
2013 BS45	2456338.41	1.00000015	0.086	0.82	11.336	HS
2013 RZ53	2456600.14	1.00000011	0.050	1.52	3.856	HS
2014 UR	2429919.90	1.00000084	0.023	8.20	−4.116	CP+HS
2015 SO2	2457295.21	1.00000011	0.108	9.20	12.145	HS+TR
2015 TC25	2563222.35	1.00000121	0.115	4.16	11.448	HS+CP
2015 XX169	2457734.05	1.00000014	0.184	7.69	19.869	HS+CP
2015 XF261	2484520.70	1.00000374	0.319	0.95	38.588	CP+HS
2015 XC352	2366077.11	1.00000040	0.140	4.87	15.793	HS+CP
2015 YA	2457370.22	1.00000075	0.280	1.78	−32.988	HS+TR
2015 YQ1	2457381.44	1.00000221	0.405	2.50	46.530	CP+HS
2016 CO246	2458132.16	1.00000011	0.125	6.39	16.201	HS+CP
2016 JA	2473372.23	1.00000201	0.270	0.09	29.382	HS
2017 DR109	2457810.31	1.00000020	0.243	2.99	−26.587	HS+CP
2017 FZ2	2457833.43	1.00000264	0.265	1.73	32.256	HS+TR
2017 SL16	2458746.73	1.00000012	0.153	8.73	−18.738	HS+CP
2018 KS	2457896.31	1.00000045	0.199	9.14	23.949	CP
2018 PK21	2487837.81	1.00000011	0.077	1.54	−8.633	HS
2018 PN22	2456718.64	1.00000011	0.028	4.40	3.160	CP
2018 UC	2530606.45	1.00000011	0.333	0.43	−38.332	HS
2019 DJ1	2433930.56	1.00000011	0.118	1.70	−15.933	HS+CP
2019 GF1	2437143.40	1.00000011	0.044	1.84	6.954	HS+TR
2019 GM1	2462423.17	1.00000011	0.073	6.70	−9.689	HS+CP
2019 HM	2557019.46	1.00000047	0.004	5.86	−2.555	CP
2019 SB6	2458763.88	1.00000017	0.267	7.21	27.634	CP
2019 VL5	2459616.44	1.00000011	0.279	1.66	30.700	HS
2019 XS	2428282.15	1.00000014	0.325	4.20	113.230	TR
2019 XH2	2493516.14	1.00000020	0.150	4.10	−18.104	CP
2019 YB4	2458851.98	1.00000018	0.194	0.47	22.618	HS
2020 CB	2501608.08	1.00000038	0.287	3.82	−32.810	TR
2020 FN3	2436661.34	1.00000091	0.209	0.94	25.719	CP
2020 GE	2460575.27	1.00000551	0.048	2.32	−7.112	CP
2020 HO5	2482334.95	1.00000064	0.023	4.73	3.727	CP
2020 KJ4	2459000.79	1.00028859	0.137	2.74	16.421	HS+TR
2020 PN1	2459453.40	1.00000011	0.125	4.95	−14.883	HS+CP
2020 PP1	2441019.81	1.00000011	0.059	5.80	6.594	HS+TR
2021 CC7	2609920.84	1.00000046	0.039	7.35	−4.577	CP
2021 EY1	2517726.61	1.00000014	0.456	5.97	54.569	CP
2021 GM1	2424782.01	1.00000256	0.043	1.53	2.700	CP
2021 JE1	2471610.72	1.00007781	0.264	0.45	−31.182	CP
2021 LF6	2459359.91	1.00000013	0.022	2.99	1.271	CP
2021 RZ3	2563353.39	1.00000083	0.054	2.18	7.606	HS+CP
2021 XV	2459547.63	1.00000567	0.323	6.79	−38.580	CP+HS

Table 5
The co-orbital objects on quasi-coplanar orbits, not in a regular TP regime, found for the Sun–Jupiter system. The values reported refer to the intersection with $u = 0$, that is the closest one to the current date, assumed to be 2021-03-21 00.00.00 (JD 2459294.50). The angular values are reported in degrees and are defined with respect to the orbital plane of the planet. The last column indicates the co-orbital dynamics detected in the given time frame (CP refers to compound, TR to transient). These co-orbital configurations are shown also in Fig. 4c.

Asteroid	t (JD)	a (au)	e	I	θ	Dynamics
2005 TS100	2472880.96	5.20366671	0.298	13.35	34.121	HS
2014 SE288	2333777.10	5.20336302	0.358	8.94	26.695	HS
2006 SA387	2436624.78	5.20336306	0.194	2.79	29.869	HS
1998 WK44	2448225.35	5.20336303	0.057	5.69	24.585	HS
2000 QV233	2453185.37	5.20336306	0.258	4.61	−32.581	HS
2002 GE195	2468467.67	5.20336514	0.191	6.53	−24.533	HS
2004 AE9	2448352.65	5.20336301	0.642	2.08	−45.845	QS
2007 EV40	2435078.29	5.20336472	0.634	3.72	78.947	QS
2009 KE31	2447987.01	5.20336303	0.172	6.43	−23.593	HS
2009 KQ31	2462775.62	5.20336306	0.089	3.77	−24.875	HS
2009 SV412	2440099.70	5.20336340	0.416	10.85	−39.691	CP
2009 UK120	2446482.25	5.20336319	0.634	0.89	74.976	HS
2009 WQ109	2476705.06	5.20336301	0.712	2.06	−52.277	QS
2010 ST19	2503334.19	5.20336330	0.110	6.18	−1.800	HS
2012 TT139	2457889.34	5.20336304	0.166	8.44	−30.646	TR
2013 NF15	2486427.97	5.20336329	0.736	1.78	−93.401	TR
2014 EC59	2460325.34	5.20336315	0.163	7.28	29.940	TR
2014 EN60	2465603.12	5.20336317	0.175	6.88	29.454	HS
2014 EL63	2461772.06	5.20336301	0.144	11.39	33.633	TR
2014 ES72	2493233.04	5.20336308	0.244	5.94	−25.510	CP
2014 ED74	2450750.08	5.20336301	0.100	7.41	24.886	HS
2014 EM82	2448567.13	5.20336301	0.047	7.62	22.004	HS
2014 EB85	2449302.04	5.20336355	0.129	9.28	20.801	HS
2014 ET119	2449327.92	5.20336305	0.145	5.94	19.498	HS
2014 EM120	2460943.70	5.20336317	0.136	4.01	28.669	HS+TR
2014 EB132	2461602.75	5.20336301	0.107	8.03	27.361	HS
2014 EF133	2419283.15	5.20336792	0.283	3.50	30.812	HS
2014 EO135	2449156.61	5.20336304	0.091	7.93	19.949	HS
2014 EG141	2449712.64	5.20336305	0.085	9.10	21.163	HS
2014 EP147	2448562.62	5.20336314	0.094	7.27	25.307	HS
2014 EA155	2449429.26	5.20336311	0.110	7.55	20.669	HS
2014 ES157	2449443.15	5.20336311	0.164	6.58	24.907	HS
2014 EY166	2449528.38	5.20336306	0.164	7.18	26.464	HS
2014 EP169	2448561.02	5.20336302	0.145	11.14	25.141	HS
2014 EG177	2449864.21	5.20336309	0.102	8.34	18.930	HS
2014 EX180	2449411.76	5.20336312	0.121	8.44	23.814	HS
2014 EA187	2449243.72	5.20336326	0.101	8.38	20.206	HS
2014 EL209	2449705.65	5.20336314	0.169	7.03	23.661	HS
2014 ET220	2449629.93	5.20336307	0.093	7.51	19.888	HS
2014 EX220	2448756.35	5.20336302	0.069	8.88	23.884	HS
2014 EJ226	2447679.67	5.20336301	0.138	9.08	28.139	HS
2014 ED239	2450381.92	5.20336302	0.082	12.00	19.677	HS
2014 EY243	2459294.68	5.21540765	0.135	8.50	33.971	HS+TR
2014 EK245	2448618.35	5.20336302	0.051	7.79	22.866	HS
2014 FP59	2462035.57	5.20339839	0.395	11.30	47.257	HS+TR
2014 OY165	2494332.56	5.20336356	0.714	4.52	−85.671	CP
2015 BB555	2438741.70	5.20336301	0.680	10.77	63.329	QS
2015 YJ22	2462187.93	5.20336303	0.558	4.00	−71.883	HS+TR
2016 CE150	2457268.76	5.20336314	0.379	1.13	48.996	HS
2016 GJ51	2461599.19	5.20336314	0.737	1.55	102.801	HS
2016 UY220	2492599.21	5.20336358	0.531	2.26	66.141	HS
2016 UG221	2473905.66	5.20339692	0.650	2.15	−73.971	HS
2016 UE223	2440247.96	5.20336303	0.660	3.66	87.896	HS
2017 QO100	2383735.18	5.20336338	0.515	8.01	−63.341	TR
2017 WJ30	2433862.33	5.20337222	0.542	8.96	60.345	HS+CP
2018 PZ27	2474081.46	5.20336304	0.657	7.78	69.511	QS
2019 AS35	2464610.62	5.20336301	0.734	1.51	−85.384	QS
2019 QU75	2442259.38	5.20336376	0.223	8.69	−24.977	QS
2020 MM5	2457519.22	5.20336301	0.576	7.27	29.890	QS
2021 PM66	2518743.99	5.20339257	0.163	17.71	−22.188	HS

References

Aksnes, K., 1985. The tiny satellites of Jupiter and saturn and their interactions with the rings. In: Szebehely, V.G. (Ed.), In: NATO (ASI) Series C, vol. 154, pp. 3–16.

Barrabés, E., Ollé, M., 2006. Invariant manifolds of L_3 and horseshoe motion in the restricted three-body problem. Nonlinearity 19, 2065–2089.

Bate, R., Mueller, D., White, J., 1971. Fundamentals of Astrodynamics. Dover Publications, Inc. New York.

Brasser, R., et al., 2004. Transient co-orbital asteroids. Icarus 171, 102–109.

Christou, A., 2000. A numerical survey of transient co-orbitals of the terrestrial planets. Icarus 144 (1), 1–20.

Ćuk, M., et al., 2012. Long-term stability of horseshoe orbits. Mon. Not. R. Astron. Soc. 426 (4), 3051–3056.

de la Fuente Marcos, C., de la Fuente Marcos, R., 2012. (309239) 2007 RW10: a large temporary quasi-satellite of neptune. Astron. Astrophys. 549, L9.

de la Fuente Marcos, C., de la Fuente Marcos, R., 2013. A resonant family of dynamically cold small bodies in the near-earth asteroid belt. Mon. Notices R. Astron. Soc. Lett. 434 (1), L1–L5.

de la Fuente Marcos, C., de la Fuente Marcos, R., 2016. Asteroid (469219) 2016 HO3, the smallest and closest earth quasi-satellite. Mon. Not. R. Astron. Soc. 462, 3441–3456.

ESA, 2022. ESA - vigil mission. https://Www.Esa.Int/Space_Safety/Vigil.

Gallardo, T., 2006. Atlas of the mean motion resonances in the Solar System. Icarus 184, 29–38.

Garfinkel, B., 1977. Theory of the Trojan asteroids. I. Astron. J. 82, 368–379.

Gibney, E., 2019. China plans mission to earth's pet asteroid. Nature.

Jin, W., et al., 2020. A simulated global GM estimate of the asteroid 469219 Kamo'oalewa for China's future asteroid mission. Mon. Not. R. Astron. Soc. 493 (3), 4012–4021.

Kinoshita, H., Nakai, H., 2007. Quasi-satellites of Jupiter. Celestial Mech. Dynam. Astronom. 98, 181–189.

Mikkola, S., et al., 2004. Asteroid 2022 VE68, a quasi-satellite of venus. Mon. Not. R. Astron. Soc. 351, L63–L65.

Minor Planet Center, 2022. MPC trojan minor planets list. https://Www.Minorplanetcenter.Net/Iau/Lists/Trojans.Html.

Murray, C.D., Dermott, S.F., 2000. Solar System Dynamics. Cambridge University Press, http://dx.doi.org/10.1017/CBO9781139174817.

Nakamura, T., et al., 2021. Science operation plan of phobos and deimos from the MMX spacecraft. Earth Planets Space 73, 227.

Namouni, F., 1999. Secular Interactions of Coorbiting Objects. Icarus (2), 293–314.

Namouni, F., Christou, A.A., Murray, C.D., 1999. Coorbital dynamics at large eccentricity and inclination. Phys. Rev. Lett. 83, 2506–2509. http://dx.doi.org/10.1103/PhysRevLett.83.2506.

NASA, 2022. JPL horizons system. https://Ssd-Api.Jpl.Nasa.Gov/Doc/Horizons.Htm.

NASA JPL Solar System Dynamics, 2022a. Planetary physical parameters. https://Ssd.Jpl.Nasa.Gov/Planets/Phys_par.Html.

NASA JPL SSD, 2022b. Approximate positions of the planets. https://Ssd.Jpl.Nasa.Gov/Planets/Approx_pos.Html.

NASA JPL SSD, 2022c. Small-body database query. https://Ssd.Jpl.Nasa.Gov/Horizons/Time_spans.Html.

NASA JPL SSD Small-Body Database, 2022. Small-body database query. https://Ssd.Jpl.Nasa.Gov/Tools/Sbdb_query.Html.

Nesvorný, D., et al., 2002. A perturbative treatment of the co-orbital motion. Celestial Mech. Dynam. Astronom. 82, 323–361.

Pousse, A., Alessi, E., 2021. A stable heliocentric disposal strategy for LPO missions, inspired by the natural co-orbital motion of Saturn's moons. In: Proceedings of the International Astronautical Congress. IAC.

Pousse, A., Alessi, E.M., 2022. Revisiting the averaged problem in the case of mean-motion resonances in the restricted three-body problem. Nonlinear Dynam. 108, 959–985.

Pousse, A., Robutel, P., Vienne, A., 2017. On the co-orbital motion in the planar restricted three-body problem: the quasi-satellite motion revisited. Celestial Mech. Dynam. Astronom. 128 (4), 383–407.

Qi, Y., Qiao, D., 2022. Stability Analysis of Earth Co-orbital Objects. Astron. J. 163 (5), 211. http://dx.doi.org/10.3847/1538-3881/ac5e2c.

Robutel, P., Gabern, F., 2006. The resonant structure of Jupiter's Trojan asteroids - I. Long-term stability and diffusion. Mon. Not. RAS 372, 1463–1482.

Robutel, P., Pousse, A., 2013. On the co-orbital motion of two planets in quasi-circular orbits. Celestial Mech. Dynam. Astronom. 117, 17–40.

Sheppard, S., et al., 2022. A deep and wide twilight survey for asteroids interior to earth and venus. Astron. J. 164 (4), 168, https://doi.org/10.3847/1538-3881/ac8cff.

Sidorenko, V., et al., 2014. Quasi-satellite orbits in the general context of dynamics in the 1:1 mean motion resonance: perturbative treatment. Celestial Mech. Dynam. Astronom. 120, 131–162.

Szebehely, V., 1967. Theory of Orbits. the Restricted Problem of Three Bodies. Academic Press, New York.

Wajer, P., 2010. Dynamical evolution of Earth's quasi-satellites: 2004 GU9 and 2006 FV35. Icarus 209, 488–493.

Wajer, P., Kròlikowska, M., 2012. Behavior of Jupiter non-Trojan co-orbitals. Acta Astron. 62, 113–131.

Wolf, M., 1906. Photographische aufnahmen von kleinen planeten. Astron. Nachr. 173, 269–270.